

Extreme Emission-Line Galaxies in the MUSE Hubble Ultra Deep Field Survey

I. del Moral-Castro^{1,2,3*}, J. M. Vílchez⁴, J. Iglesias-Páramo^{4,5}, and A. Arroyo-Polonio⁴

¹ Instituto de Astrofísica, Facultad de Física, Pontificia Universidad Católica de Chile, Campus San Joaquín, Av. Vicuña Mackenna 4860, Macul, Santiago, Chile, 7820436

² Kapteyn Astronomical Institute, University of Groningen, PO Box 800, 9700 AV Groningen, The Netherlands

³ Facultad de Física, Universidad de La Laguna, Avda. Astrofísico Fco. Sánchez s/n, 38200, La Laguna, Tenerife, Spain

⁴ Instituto de Astrofísica de Andalucía – CSIC, Glorieta de la Astronomía s/n, 18008 Granada, Spain

⁵ Centro Astronómico Hispano en Andalucía, Observatorio de Calar Alto, Sierra de los Filabres, 04550 Gérgal, Spain

Received ; accepted

ABSTRACT

Aims. We apply a methodology to build a sample of extreme emission line galaxies (EELGs) using integral field spectroscopy data. In this work we follow the spectroscopic criteria corresponding for EELG selection and use the MUSE Hubble Ultra-Deep field survey, which includes the deepest spectroscopic survey ever performed.

Methods. Objects in the primary (extended) sample were detected requiring a rest-frame equivalent width $EW_o \geq 300 \text{ \AA}$ ($200 \text{ \AA} \leq EW_o \leq 300 \text{ \AA}$) in any of the emission lines of $[OIII]\lambda\lambda 3726, 29$, $[OIII]\lambda\lambda 5007, 4959$, or $H\alpha$. A detailed closer inspection of the spectra of the candidates selected has been performed on a one by one basis, in order to confirm their classification. For this sample, the line fluxes, physical properties and chemical abundances of the EELGs have been derived as well as their spatially resolved structure and kinematics.

Results. Four (five) of the galaxies in the primary (extended) sample, $\sim 57\%$ ($\sim 83\%$), were spatially resolved. Three (none) of them present a clear pattern compatible with rotation. We have shown how our entire EELGs sample share the same loci defined by high-redshift galaxies ($z \approx 6-8$) for the mass-metallicity relation, illustrating their role as local analogs.

Key words. galaxies: evolution – galaxies: star formation – galaxies: starbursts

1. Introduction

Galaxies hosting strong events of star formation can provide keys for our understanding of early galaxy evolution, since such extreme star-forming objects are expected to be more frequent towards the first epochs of the Universe. In this sense, these highly star-forming galaxies provide useful windows to the high- z Universe, allowing us to study the photon budget required for its re-ionization (e.g. Stark 2016; Dayal & Ferrara 2018). The nature, properties and prevalence of these galaxies at the Epoch of Reionization (EoR) remain to be fully understood.

All these galaxies have been named as a class as extreme emission line galaxies (EELGs) since their (optical) spectra show very strong emission lines with extreme equivalent width (EW). EELGs host a considerable number of massive young star forming systems producing a substantial amount of photoionising radiation. This radiation is absorbed by the surrounding metal-poor gas (e.g., Ravindranath et al. 2020). Since the gas is expected to have a perforated irregular distribution, hard ionising radiation could escape (e.g. Bergvall et al. 2006; Izotov et al. 2016; Fletcher et al. 2019; Pérez-Montero et al. 2020). It turns these systems into perfect laboratories for the study of LyC escape. Therefore, the discovery and characterisation of local EELG analogs give us a way to gain more insight about first moments of galaxy evolution when leakage of LyC photons from EELGs provided a major contribution to the EoR photon bud-

get (e.g. Erb et al. 2016; Yang et al. 2017a; Naidu et al. 2022; Matthee et al. 2022).

EELGs present spectra with very high EW of $[OIII]$ and $H\beta$ emission lines, and it has been found that these galaxies use to be also strong $Ly\alpha$ emitters (Tang et al. 2021). On the other hand, most typical LyC leakers presenting a very high $EW(Ly\alpha)$ are frequently found among Green Pea galaxies, an outstanding family among the prototypes of EELGs (Izotov et al. 2016, 2018; Pérez-Montero et al. 2021).

As of today, observational studies have discovered thousands of EELGs but most searches have produced a mixed bag of denominations, typically inspired by their compact optical appearance and/or colour in plates; examples of these are Green Peas, Blue Berries, ELDots/ $H\alpha$ Dots, or SDSS extreme HII galaxies and their cohorts, to cite a few (e.g. Terlevich et al. 1991; Cardamone et al. 2009; Amorín et al. 2010, 2012; Bekki 2015; Yang et al. 2017b; Salzer et al. 2020), all illustrating how EELG selection can depend on the redshift range explored and the exact criteria and technique applied. The search for EELGs is somewhat complementing the historical searches for blue galaxies of very compact morphology that were identified and analyzed in pioneering works since the middle of the last century (e.g. Haro 1956; Zwicky 1966; Markarian 1967). However, it is important to emphasize here that a large majority of EELG searches performed so far were based on broad-band photometry data, thus avoiding direct spectroscopic or narrow-band based selection based on emission lines which still remains scarce (see e.g. Indahl et al. 2021; Lumberras-Calle et al. 2022; Iglesias-Páramo

* E-mail: ignaciodelmoralcastro.astro@gmail.com

et al. 2022). This situation may have somehow supported the persistence of systematics and/or obvious bias in current samples of EELG, given the typical very faint continua and the strong emission lines of these galaxies. A clear example are the differences in the number and occurrence of these objects. Paalvast et al. (2018) explored galaxies with extreme [OIII]/[OII] ratios combining data from several MUSE Guaranteed Time Observing (GTO) programmes ($0.28 < z < 0.85$) founding 15 of these systems in their sample (3.7% of their total sample). Cardamone et al. (2009) imposing conditions on r_{SDSS} , redshift, optical colours, and morphology reported a spatial density of Green Peas of approximately 2 per square degree, a critical benchmark in EELG studies. In the local Universe, Yang et al. (2017a) found a density of 0.003 EELGs per square degree for ‘blueberries’ in the local universe ($z \leq 0.05$), while Lumberras-Calle et al. (2022) identified 466 EELGs within 2000 square degrees, equivalent to a density of about 0.23 per square degree, in the J-PLUS survey ($z \leq 0.06$). Furthermore, Amorín et al. (2015) reported 165 EELGs in the 1.7 square degree area covered by the zCOSMOS-bright survey, indicating a density of approximately 97 per square degree in the redshift range $0.11 \leq z \leq 0.93$. As Iglesias-Páramo et al. (2022) noted precise comparisons among different works are prevented by the different selection criteria and observational limits of each sample.

There is not a clear limit for the rest-frame equivalent width (E_{Wo}) to define a galaxy as an EELG. In this work, we use a similar definition for EELGs to that used by Iglesias-Páramo et al. (2022), i.e. objects that show at least one emission line ([OII] $\lambda\lambda$ 3726,3729, [OIII] $\lambda\lambda$ 4959,5007 or H α) with $E_{Wo} \geq 300 \text{ \AA}$.

Nevertheless, we are aware that previous works have assumed different selection limits for EELGs (e.g. Amorín et al. 2015; Salzer et al. 2020; Iglesias-Páramo et al. 2022 and references therein); therefore for the sake of consistency with previous works, we have enlarged our search producing an extended sample including all sources presenting $E_{Wo} \geq 200 \text{ \AA}$. In this way, we gain consistency in order to compare with literature work, and could examine the behaviour of the main properties of EELGs around the adopted E_{Wo} limit; an exercise especially relevant when looking for any possible evolution through redshift.

In this work we take advantage of the exceptional depth and quality of the recent MUSE Hubble Ultra-Deep field survey data release (HUDFS; Bacon et al. 2023) to carry out a purely spectroscopic search for EELG with MUSE. EELGs usually show a compact appearance although some low surface brightness structure can be seen for some of them (see Appendix A from Iglesias-Páramo et al. 2022 for examples). Here, we have been able to spatially resolve the ionization structure and the gaseous kinematics of this type of objects. This paper is organised as follows. In the next section we summarise the observations and criteria to select the sample. Section 3 shows the basic properties of our EELG candidates. The results and discussion are presented in Section 4. The main conclusions are summarised in Section 5.

2. Data and sample

2.1. MUSE Hubble Ultra-Deep Field

The MUSE instrument is a powerful tool for optical (4750–9350 Å) spectroscopic studies thanks to a combination of a wide field of view (FoV) of 1'x1' with a spatial sampling of 0.2"x 0.2" per spaxel and high resolving power (ranging from $R \sim 1800$ in the blue to $R \sim 4000 \text{ \AA}$ in the red). Our study is

based in the second data release (DR2) of the MUSE Hubble Ultra-Deep Field surveys (Bacon et al. 2023), which includes the deepest spectroscopic survey ever performed. With an achieved depth of 141 hours and a field of view of 1 arcmin of diameter, it is a key addition to the previous MUSE spectroscopic survey data release (Bacon et al. 2017; Inami et al. 2017; DR1, a $3 \times 3 \text{ arcmin}^2$ mosaic of nine MUSE fields at a 10-hour depth and a single $1 \times 1 \text{ arcmin}^2$ at 31-hour depth) in the Hubble ultra-deep field (Beckwith et al. 2006; HUDF) area. This second data release (DR2) incorporates the previous ones reprocessed with the same tools and methodology, providing a homogeneous data set of deep spectroscopic observations in the HUDF region.

In addition to the calibrated data, the data cubes have an extension with the propagated variance estimate, which is used in the line fitting process (see Sect. 3.1). Reduced and calibrated data cubes, the source catalogues and an interactive browser are available to the public through the AMUSED web interface¹.

2.2. Sample selection

Our selection process begins by analysing the information offered by the AMUSED interface. The main catalogue gives a summary of source properties and the final datacubes and associated images (e.g. Hubble images) are public for each object. We follow the criteria in Iglesias-Páramo et al. (2022) and define our primary sample of EELG as those objects that show at least one emission line with $E_{Wo} \geq 300 \text{ \AA}$. We use the E_{Wo} measured by Bacon et al. (2023) using the python code pyPlatefit². Briefly, pyPlatefit is an improved Python-based version of the PLATEFIT IDL software (Brinchmann et al. 2004) developed to fit MUSE data. It performs a stellar continuum fitting using a simple population model (Bruzual & Charlot 2003) and then fits the emission lines with gaussian profiles after subtracting the continuum. To characterise the local continuum, pyPlatefit masks the emission lines and uses windows of 50 Å on the left and right.

Using these criteria, of the 2221 catalogued objects, we found a total of 2, 5 and 3 galaxies presenting rest-frame $E_{Wo} \geq 300 \text{ \AA}$ in [OII], [OIII] and H α , respectively. One of these objects presents $E_{Wo} \geq 300 \text{ \AA}$ in two lines ([OIII] and H α). Thus, we selected 9 candidates (ID 91, 891, 895, 1795, 2478, 2532, 6465, 7373 and 7601) fulfilling the criteria for our primary EELG sample. A detailed closer inspection of the spectra of these 9 candidates has been performed on a one by one basis. In doing so, we have found that the spectra of two of the candidates (ID 1795 and 7601) show low signal to noise ratio (SNR) over the entire wavelength range, giving non realistic lines fitting in the AMUSED database. Therefore, these two candidates were discarded from our EELGs primary sample. Table 1 shows the basic properties of the sample; these include quantities extracted from AMUSED (MUSE ID, coordinates, redshift, magnitude in the HST F775W band, stellar mass, star formation rate, line of detection, line flux, corresponding luminosity³ and rest frame E_{Wo}), and measurements of this work for line flux and rest frame E_{Wo}. All these relevant spectrophotometric properties will be considered in the discussion.

Furthermore, as commented before, we have produced also an extended EELG sample with sources presenting $200 \text{ \AA} \leq$

¹ <https://amused.univ-lyon1.fr/>

² <https://pyplatefit.readthedocs.io/en/latest/tutorial.html>

³ Note that this luminosity is not corrected by the extinction of each galaxy. See Sect. 4.1

$E_{\text{Wo}} \leq 300 \text{ \AA}$ in at least one of the lines considered above ([OII] $\lambda\lambda 3726, 3729$, [OIII] $\lambda\lambda 4959, 5007$ or $H\alpha$). Using these extended criteria, we found a total of 3, 8 and 1 galaxies showing $200 \text{ \AA} \leq E_{\text{Wo}} \leq 300 \text{ \AA}$ in [OII], [OIII] and $H\alpha$, respectively. One of the objects detected in [OIII] presents a $E_{\text{Wo}} \geq 300 \text{ \AA}$ in $H\alpha$ (ID 7373) and one object shows $200 \text{ \AA} \leq E_{\text{Wo}} \leq 300 \text{ \AA}$ in both [OIII] and $H\alpha$ (ID 6474). Therefore, giving 10 candidates (ID 1093, 1426, 1561, 1699, 6474, 6865, 1863, 7105, 7985, 8000) for the extended EELG sample. We have performed a detailed closer inspection of the spectra of these 10 candidates, as done for the primary sample. Following the same criteria, we end up discarding 4 galaxies (ID 1863, 7105, 7985 and 8000). The galaxies selected for our extended EELG sample are listed in Table 2.

Figure 1 shows the distribution of redshift, mag_{F775W} , $E_{\text{Wo}}([\text{OIII}]\lambda 4959)$ ⁴ and $L_{[\text{OIII}]}$. These candidates expand the ranges: $0.1 < z < 0.9$, $22 < \text{mag}_{F775W} < 28$, $200 \text{ \AA} < E_{\text{Wo}} < 1200 \text{ \AA}$ and $41.9 \leq \text{Log}(L_{[\text{OIII}]} / \frac{\text{erg}}{\text{s}}) \leq 44.2$, respectively. We can see that both, primary and extended, samples share the same range of basic properties. Note that the low number of objects in our sample is totally expected based on reported densities of similar objects in the literature (e.g. Iglesias-Páramo et al. 2022). Furthermore, we do not find systems with redshift ≤ 0.1 being consistent with previous works in the local Universe (e.g. Yang et al. 2017b; Lumberras-Calle et al. 2022).

3. Properties of the EELG sample

3.1. EELG spectra and line fluxes

Figure 2 shows the spectra of both EELG primary and extended samples. All the selected objects present characteristic spectra of strong emission line galaxies, consisting of a faint continuum and very prominent emission lines.

As we indicated in Sec. 2, our sample selection is based in the information given by the AMUSED web interface and the fittings performed by Bacon et al. (2023). The equivalent width values depend on the continuum level and this can be difficult to characterise. Therefore, we decide to re-evaluate the E_{Wo} values of our samples to confirm the EELG classification. Emission-line fitting was performed with `pyPlatefit` including improvements with respect the previous fittings. Firstly, we use the parameter `z1ter`, which allow to a second iteration improving the fitting. Secondly, we perform 100 Monte Carlo simulations to compute uncertainties following standard procedures in full spectra fitting techniques (e.g. del Moral-Castro et al. 2019, 2020; Bittner et al. 2019; Domínguez-Gómez et al. 2023 and references there). Briefly, we derive these uncertainties creating multiple realisations of the original spectrum adding random noise consistent with the quality of the observed spectrum to the best fit and running `pyPlatefit` again. The considered errors are the standard deviation of the 100 recovered values. Tables C.1 and D.1 presents the fluxes measured for the emission lines for the primary and extended samples.

Thirdly, three objects (MUSE ID 91, 7373 and 1093) present a cut in the spectrum (from ~ 5800 to $\sim 5970 \text{ \AA}$). Then, to avoid possible problems with the fitting to the continuum, we fit the wavelength range from 6000 to 9300 \AA . As for the rest of objects, the whole wavelength range was considered (4750 - 9300 \AA). We notice that the object 2478 presents a

very high $E_{\text{Wo}}([\text{OIII}]\lambda 5007)$. This value seem to be too high, since the $F([\text{OIII}]\lambda 4959) / ([\text{OIII}]\lambda 5007)$ is $\sim 1/3$. Therefore, $E_{\text{Wo}}([\text{OIII}]\lambda 5007)$ should be $\sim 3 \cdot E_{\text{Wo}}([\text{OIII}]\lambda 4959)$. However, it is ~ 30 . Through an inspection of the line catalogue given by AMUSED, we found that the continuum associated to the [OIII] $\lambda 5007$ emission line is almost an order of magnitude less than the continuum level of the [OIII] $\lambda 4959$ emission line. However, $F_{\text{cont}}([\text{OIII}]\lambda 4959) / F_{\text{cont}}([\text{OIII}]\lambda 5007) \sim 1$ for the rest of the objects. Therefore, we decide using the continuum level of the [OIII] $\lambda 4959$ emission line to compute the $E_{\text{Wo}}([\text{OIII}]\lambda 5007)$ of MUSE ID 2478.

Finally, we studied the effect of the window width used by `pyPlatefit` to characterise the local continuum⁵ on the E_{Wo} values. We used `pyPlatefit` changing the internal configuration to use windows of 100 and 200 \AA confirming the EELG classification except for the object MUSE ID 7373, where the E_{Wo} values for windows of 100 and 200 \AA are 102 ± 11 and 106 ± 7 , respectively. Therefore, we added a flag of caution for this galaxy in Table 1.

3.2. Spectroscopic and spatially resolved properties

Figure 3 presents an example of photometric and spectroscopic properties derived for the galaxy ID 891. The upper row shows the HST 775W and MUSE white-light images, as well as the MUSE spectrum with an inset zooming around the $H\gamma$ and [OIII] $\lambda 4363 \text{ \AA}$ emission lines. In the bottom row we present the spatially resolved spectroscopic and kinematic information of the galaxy which will be discussed in 4.2. Emission-line fitting was performed using `pyPlatefit` `spaxel` by `spaxel`. The velocity field shows a clear pattern of rotation similar to those of nearby disc-galaxies (i.e. Barrera-Ballesteros et al. 2014; del Moral-Castro et al. 2019). Only spaxels with significant line detections ($S/N > 6$) are shown. We checked that the results are not contingent upon the choice of the minimum signal to noise ratio S/N by repeating the analysis with different thresholds (3, 6, and 9). We prefer to stick to $S/N=6$ to preserve the best possible spatial resolution for this analysis combining with a robust selection. Appendices A and B show similar images for the the EELG primary and extended samples, respectively.

4. Results and discussion

4.1. Physical properties and chemical abundances

In order to compute the physical properties of the galaxies of our EELG sample⁶ we have followed the expressions in Pérez-Montero (2017). The Balmer decrement was used for the derivation of the reddening coefficient $C(H\beta)$ assuming Case B approximation for electron temperature 15000 K and density 100 cm^{-3} (Storey & Hummer 1995), and the extinction law by Cardelli et al. (1989) with $R_V=3.1$. In any case, no relevant change is expected if the exact electron temperature and density of each object are used. Whenever possible, the ratio of the bright Balmer

⁵ Although, the broad-band Hubble Space Telescope (HST) observations are deeper than those of MUSE, the filter widths (F606W: 4632.15 - 7179.43 \AA and F775W: 6801.41 - 8630.74 \AA , see Fig. 1 from Bacon et al. 2023) are too large to ignore the presence of non-uniform spectral energy distribution (SED) components and other emission features in the characterisation of the local continuum.

⁶ A closer inspection of all individual line profiles confirmed the presence of narrow lines in all the sources, discarding AGN contamination. Furthermore, the BPT diagram was performed for three of them locating the galaxies in the star formation region.

⁴ Note that two galaxies (MUSE ID: 891 and 7373) are included in the primary sample performing its condition in $E_{\text{Wo}}_{H\alpha}$, though their $E_{\text{Wo}}([\text{OIII}])$ are lower than 300 \AA .

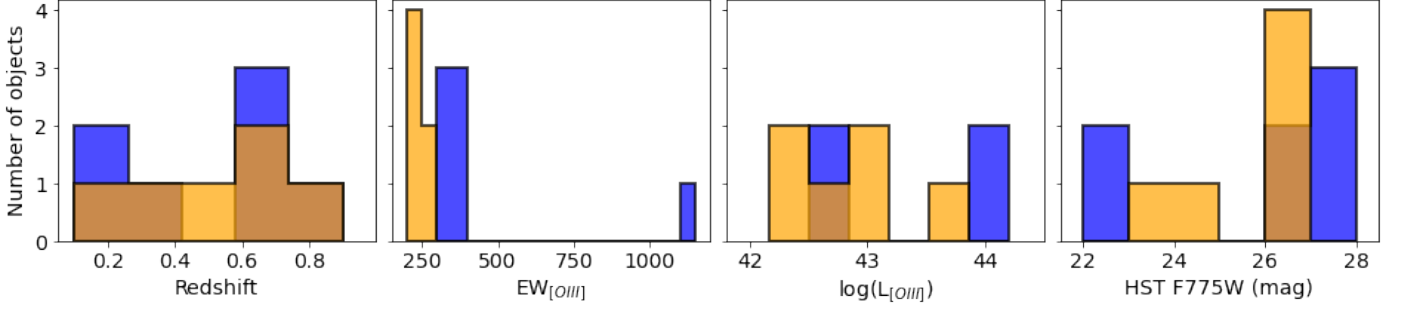


Fig. 1. Histograms of the distribution of properties of the sample of EELGs. See the text for details.

MUSE ID	Ra (AMUSED) (deg)	Dec (AMUSED) (deg)	z (AMUSED)	mag _{F775W} (AMUSED)	log Mass (AMUSED) $\log(\frac{M_{\text{gas}}}{M_{\odot}})$	log SFR (AMUSED) $\log(\frac{M_{\odot}}{\text{yr}})$	Line	F (AMUSED) $(10^{-20} \frac{\text{erg}}{\text{cm}^2})$	LogL (AMUSED) $(\frac{\text{erg}}{\text{s}})$	Cont (AMUSED) $(10^{-20} \frac{\text{erg}}{\text{cm}^2 \text{Å}})$	EWo (AMUSED) (Å)	F (this work) $(10^{-20} \frac{\text{erg}}{\text{cm}^2})$	Cont (this work) $(10^{-20} \frac{\text{erg}}{\text{cm}^2 \text{Å}})$	EWo (this work) (Å)
(1)	(2)	(3)	(4)	(5)	(6)	(7)	(8)	(9)	(10)	(11)	(12)	(13)	(14)	(15)
91	53.1625	-27.7803	0.72	26.18	8.26	-1.27	[OIII]λ5007	4098	42.82	11.89	345	4099±6	11.89±0.45	345±13
891	53.1957	-27.7878	0.23	22.21	8.44	-0.54	Hα	67946	44.04	218.37	311	67942±15	218.37±0.46	311±1
895	53.1447	-27.7854	0.25	22.47	8.6	-0.64	[OIII]λ5007	92674	44.17	255.45	363	92673±17	255.45±1.02	363±2
							Hα	57498	43.96	173.54	331	57500±9	173.54±0.46	331±1
2478	53.1839	-27.7954	0.73	27.85	7.19	-2.11	[OIII]λ4959	583	41.97	1.55	375	583±3	1.55±0.26	375±98
							[OIII]λ5007	2065	42.52	0.18	11478 ^k	2065±3	1.55±0.26	1332±224
2532	53.1497	-27.8093	0.75	27.91	7.44	-1.63	[OIII]λ5007	492	41.9	1.27	387	492±5	1.27±0.37	386±97
6465	53.1942	-27.7854	0.72	26.15	-	-	[OIII]λ5007	668	42.03	1.85	362	668±6	1.85±0.46	362±89
7373	53.1542	-27.7867	0.28	27.89	6.85	-2.43	Hα	102	41.21	0.33	307 ^k	102±2	0.33±0.11	309±100

Table 1. Basic properties of the EELG primary sample candidates. (1) MUSE source identifier; (2) Right ascension (J2000.0); (3) Declination (J2000.0); (4) Redshift; (5) Magnitude in HST F775W; (6) Stellar mass; (7) Star formation rate; (8) Detected emission line with ≥ 300 Å; (9) Flux of the emission feature; (10) Luminosity of the emission feature; (11) Flux of the continuum level; (12) Rest frame equivalent width of the emission feature (^k uncertain value); (13) Flux of the emission feature (measured in this work); (14) Flux of the continuum level (measured in this work); (15) Rest frame equivalent width of the emission feature (measured in this work).

MUSE ID	Ra (AMUSED) (deg)	Dec (AMUSED) (deg)	z (AMUSED)	mag _{F775W} (AMUSED)	log Mass (AMUSED) $\log(\frac{M_{\text{gas}}}{M_{\odot}})$	log SFR (AMUSED) $\log(\frac{M_{\odot}}{\text{yr}})$	Line	F (AMUSED) $(10^{-20} \frac{\text{erg}}{\text{cm}^2})$	LogL (AMUSED) $(\frac{\text{erg}}{\text{s}})$	Cont (AMUSED) $(10^{-20} \frac{\text{erg}}{\text{cm}^2 \text{Å}})$	EWo (AMUSED) (Å)	F (this work) $(10^{-20} \frac{\text{erg}}{\text{cm}^2})$	Cont (this work) $(10^{-20} \frac{\text{erg}}{\text{cm}^2 \text{Å}})$	EWo (this work) (Å)
(1)	(2)	(3)	(4)	(5)	(6)	(7)	(8)	(9)	(10)	(11)	(12)	(13)	(14)	(15)
1093	53.1763	-27.7809	0.54	24.87	7.92	-0.98	[OIII]λ5007	5371	42.93	22.79	236	5364±9	22.79±0.38	235±4
1426	53.1473	-27.8008	0.28	26.05	7.07	-2.06	[OIII]λ5007	2485	42.6	8.51	292	2485±5	8.51±0.29	292±10
1561	53.153	-27.7937	0.73	26.41	8.1	-1.3	[OIII]λ5007	1450	42.37	5.72	254	1450±6	5.72±0.40	254±18
1699	53.154	-27.8052	0.67	26.70	7.93	-1.26	[OIII]λ5007	905	42.16	3.98	228	905±5	3.98±0.24	228±14
6474	53.1866	-27.7902	0.12	23.20	-	-	[OIII]λ5007	26044	43.62	105.11	248	26044±8	105.11±0.39	248±1
							Hα	15343	43.39	73.78	208	15343±7	73.78±0.48	208±1
6865	53.1604	-27.7752	0.83	26.60	-	-	[OIII]λ5007	6276	43.00	25.73	244	6276±3	25.73±0.24	243±2

Table 2. Same as Table 1 for the EELG extended sample candidates.

lines H α /H β has been used. When the flux measurement of H α (ID 1426) or H β (ID 6465) is uncertain, or H α is not observed (ID 2478). The C(H β) values for all the EELGs are presented in Table 3. After inspection of the errors of the flux of the Balmer lines considered above (see Appendices C and D), a formal 20% relative error, face value, has been adopted for C(H β).

For two galaxies (ID 2478, ID 6465) the computed C(H β) was zero or slightly negative, though consistent to within the errors with the adopted value of C(H β)=0. A C(H β)=0 was adopted also for ID 2532 since only one Balmer line, H β , was measured for this galaxy. In what follows, all the fluxes used for the derivation of the physical properties and chemical abundances of the selected EELGs have been reddening corrected accordingly.

Overall, the extinction values derived for our sample of EELGs are low, typically C(H β) \approx 0.1 ($A_V \approx$ 0.22), and the maximum around $A_V \approx$ 0.45, whereas a good fraction of the sample shows values consistent with no extinction. This result, -given the negligible Galactic extinction, (Schlafly & Finkbeiner 2011)-would translate into a low (or very modest) dust component associated to our EELGs, somewhat expected for low metallicity (dwarf) galaxies.

For seven galaxies the flux in the auroral [OIII]λ4363 temperature sensitive line has been measured with good signal to noise, illustrating the high quality of the data. Therefore we have performed a direct calculation of their electron temperature, with important implications for the chemical abundance derivation. We have followed Pérez-Montero (2017) for the computation of the T[OIII] electron temperature using the ([OIII]λ5007 + [OIII]λ4959)/[OIII]λ4363 line ratio. The values of T[OIII] obtained, along with their corresponding errors derived via error propagation from the measured flux error, are presented in Table 3. The T[OIII] electron temperatures are high, going from 1.3 10^4 K to over 20 10^4 K; these temperature values being typically found in low metallicity star-forming galaxies (e.g. Amorín et al. 2015; Kehrig et al. 2016; Izotov et al. 2019; Pérez-Montero et al. 2021).

The electron density, N_e , has been derived using the line ratios from the [OII]λ3726,3729 and [SII]λ6717,6731 doublets whenever observed (redshift permitting, see Fig. 5 for an example), being both line doublets resolved in the MUSE data. For galaxies ID 91, 6465, 1093, 1426, 1561, 1699, 6865, we have measurements of the [OII]λ3726,3729 doublet; whereas the [SII]λ6717,6731 doublet is measured for ID 891, 895, 6474.

For three galaxies, ID 2478, 2532, 7373, we have no information to derive their electron density. We assume a electron temperature of 10^4 K (Sanders et al. 2016; Harshan et al. 2020). After a close inspection of the measured flux errors, in this work we have adopted a formal relative error for N_e of 20%, face value, and value of the low density limit for $N_e \leq 50 \text{ cm}^{-3}$. The electron densities derived for our EELG galaxies are shown in Table 3. These values of electron density indicate that most galaxies of the sample have a low density, and N_e in four of them being consistent with the low density limit. However, for three galaxies, ID 1699, 6474, 6865, substantially high electron densities are derived, with $N_e \approx 500$ to 600 cm^{-3} . Interestingly, two of them, ID 6474 and ID 6865, show the highest electron temperatures derived.

After obtaining the physical properties of the galaxies above we have derived their metallicity using the spectroscopic information gathered. We have calculated the oxygen chemical abundance of the ionized gas of these EELGs, as a direct measurement of their gas metallicity. To do so we proceed as follows:

1. For those galaxies (ID 91, 1093⁷, 6865) for which we have measurements of [OII] $\lambda\lambda 3726, 3729$ and [OIII] $\lambda\lambda 5007, 4959$ flux, together with the electron temperature $T[\text{OIII}]$, we can perform a direct derivation of the ionic O^+/H^+ and O^{++}/H^+ abundances, adding them up to derive the total oxygen abundance, expressed $12+\log(\text{O}/\text{H})$. For this calculation a two ionization zones scheme has been adopted following Pérez-Montero (2017), using $T[\text{OIII}]$ for the O^{++} zone, and estimating the O^+ zone temperature, $T[\text{OII}]$. The $12+\log(\text{O}/\text{H})$ of these galaxies, along with their corresponding errors estimated from error propagation of line fluxes and temperature, are quote in Table 3.
2. For those galaxies (ID 891, 895, 2478, 6474) for which we have derived the electron temperature, $T[\text{OIII}]$, but no [OII] $\lambda\lambda 3726, 3729$ lines are measured, we can not proceed with the direct method as above. In these cases we rely on the anti-correlation between the total oxygen abundance of the ionized gas and its electron temperature, as observed in Amorín et al. (2015); a direct, theoretically expected, consequence of the cooling of the ionized gas via oxygen lines. The values of $12+\log(\text{O}/\text{H})$ for these galaxies, along with the corresponding statistical error ± 0.08 dex, have been derived following the expression in Amorín et al. (2015), and are presented in Table 3. For the sake of comparison, we have derived $12+\log(\text{O}/\text{H})$ also for the three galaxies treated with the direct method above, giving a very good agreement within the errors.
3. For the rest of the galaxies we only have flux measurements of [OII] $\lambda\lambda 3726, 3729$ and [OIII] $\lambda\lambda 5007, 4959$ lines, for ID 6465, 1426, 1561, 1699, or even only [OIII] $\lambda\lambda 5007, 4959$ for ID 2532, 7373. In this third case, in order to determine the oxygen abundance we have to rely on an empirical calibration of abundance based on bright lines. Among the empirical calibrations, the one based on the R_{23} parameter, originally defined by Pagel et al. (1979) as $R_{23} = ([\text{OII}]\lambda\lambda 3726, 3729 + [\text{OIII}]\lambda\lambda 5007, 4959)/\text{H}\beta$ stands out as a useful and robust tool against possible ionization structure effects (e.g. Relaño et al. 2010; Kehrig et al. 2016). In this work we have made use of the R_{23} calibration (Izotov et al. 2019) to derive the oxygen abundance $12+\log(\text{O}/\text{H})$. Though, the R_{23} calibration is bi-valuated and

additional information is required to choose the appropriate branch, thus we have applied it as in Williams et al. (2023), selecting the low metallicity regime taking into account the high [OIII] $\lambda\lambda 5007, 4959/[\text{OII}]\lambda\lambda 3726, 3729$ measured for the EELG galaxies (e.g. Sanders et al. 2016). The derived $12+\log(\text{O}/\text{H})$ abundances and their corresponding statistical errors of ± 0.1 dex are presented in Table 3. We also show the values of R_{23} when available, or $\log \text{O}_3 = [\text{OIII}]\lambda\lambda 5007, 4959/\text{H}\beta$ when [OII] $\lambda\lambda 3726, 3729$ lines are not measured.

It has been reported that the ionised interstellar medium in some extreme emission line galaxies could be experiencing density bounded conditions (e.g. Jaskot & Oey 2013). These objects would show extreme [OIII] $\lambda\lambda 5007, 4959/[\text{OII}]\lambda\lambda 3737, 29$ flux ratios (typically ≥ 40) suggestive of the presence of non-standard conditions which may complicate the applicability of abundance calibrations. The abundance calibration applied in this work is selected from Izotov et al. (2019) and it was specifically derived for the class of extreme emission line low metallicity galaxies studied here. All sample galaxies for which the empirical calibration has been applied present moderate to low values of the [OIII] $\lambda\lambda 5007, 4959/[\text{OII}]\lambda\lambda 3737, 29$ ratio (see Tables C.1, D1), hence any potential effect associated to density bounded conditions is expected to be minor. The analysis of the oxygen abundances derived for our EELG sample indicates that these galaxies are all metal poor, with $7.35 \leq 12+\log(\text{O}/\text{H}) \leq 8.05$, showing four of them a metallicity below 0.1 solar. The very low metallicities obtained in our search for EELGs have important implications for their characterization as local analogs of the earliest star-forming galaxies.

4.2. Kinematical properties, structure and velocity maps

By inspecting the kinematics maps presented in Sec. 3.2, we can separate our sample in three different classes:

1. *Resolved with kinematic pattern*⁸: galaxies spatially resolved that show a clear pattern of rotation (i.e. presence of a disc, with the velocity increasing outward). About ~43% of EELGs in the primary sample are in this class:
 - ID 891: The HST F775W continuum image reflects a non-nuclear shape, with several high-surface brightness knots connected by a diffuse low-surface brightness component. This structure is not shown in the MUSE white light image (given the lower spatial resolution), which present a head-tail shape (i.e. a main bright star-forming clump located at the centre of the image and a low-surface brightness tail). The SNR map shows its highest values in the inner galaxy, though peaking slightly south of the flux maximum likely a consequence of the different line profile shapes and the higher velocity dispersion measured. The ionised gas velocity field presents a clear rotating disk structure, showing higher values in the region corresponding to the knots identified in the HST image. Note that these knots could be reminiscent of the structures seen in tidal dwarf and/or cometary galaxies (e.g. Lagos et al. 2016; Roche et al. 2023). These galaxies are usually considered the result of a tidal process or interactions of disk galaxies. No apparent companion is envisaged in this Figure, however further investigation on its true nature is beyond the scope of this paper.

⁷ A second fitting in the rest-frame 4000-5800Å was performed to fit the [OII] $\lambda\lambda 3726, 3729$ doublet.

⁸ Note that this class presents significantly larger velocity amplitudes.

ID	C(H β)	Te([OIII]) (10 ⁴ K)	Ne (cm ⁻³)	logR ₂₃ (logO ₃)	12+log(O/H)	Notes
91	0.11	1.65±0.04	≤ 50	0.89	7.72±0.03 [7.75]	(b) P
891	0.17	1.45±0.02	73	(0.76)	7.93±0.08	(a) P
895	0.18	1.38±0.01	75	(0.82)	7.99±0.08	(a) P
2478(★)	0.00	1.49±0.20	-	(0.95)	7.89±0.08	(a) P
2532(&)	0.00	-	-	(0.77)	-	(d) P
6465	0.00	-	90	1.03	7.77±0.10	(c) P
7373	0.22	-	-	(0.14)	-	(d) P
1093	0.09	1.31±0.12	≤ 50	0.81	7.90±0.10 [8.05]	(b) E
1426	0.20	-	≤ 50	0.75	7.47±0.10	(c) E
1561	0.13	-	≤ 50	0.83	7.58±0.10	(c) E
1699	0.10	-	544	0.77	7.51±0.10	(c) E
6474	0.13	1.69±0.06	496	(0.83)	7.72±0.08	(a) E
6865	0.12	2.08±0.05	557	0.76	7.38±0.02 [7.37]	(b) E

Table 3. Physical properties and chemical abundances.(★): H β flux measurement uncertain.(&): Only H β line flux measured; C(H β)=0 assumed.

Notes (Column 7):-

(a): Oxygen abundance derived from Te([OIII]) following Amorín et al. (2015) relation; expected ±0.08 dex statistical error.

(b): Oxygen abundance from the direct method; the abundance derived using (a) is also given in [] for comparison.

(c): Oxygen abundance from R₂₃ empirical calibration (Izotov et al. 2019; Williams et al. 2023); expected ±0.10 dex statistical error.

(d): No oxygen abundance derived; only [OIII] nebular line measured.

P: primary EELG sample; E: extended EELG sample.

- *ID 895*: The HST image shows a elongated shape, also reflected by the MUSE white light image. The [OIII] SNR map shows a nuclear shape while the H α map also presents an elongated shape with the highest values peaking slightly south of the flux maximum. Both [OIII] and H α flux maps present a nuclear shape peaking at the centre of the galaxy. The [OIII] and H α velocity field show clear rotation disk structures.
 - *ID 91*: The HST F775W image present a nuclear shape. This shape is also shown in the MUSE white light, SNR and flux maps. The [OIII] velocity field show a rotating pattern.
2. *Resolved without kinematic pattern*: galaxies spatially resolved but, unlike the previous category, do not show a rotation pattern. This class represents ~14% and ~83% of our EELGs (ID: 2478) and extended samples, respectively (ID: 1093, 1426, 1561, 6474 and 6865). The HST F775W images reflect a nuclear shape, except for the ID 6474 object, which present a elongated shape with a low-surface brightness tail. The nuclear shape is also presented in the MUSE white light, SNR and flux maps for the six galaxies.
3. *Not resolved*: galaxies whose structure can not be resolved. About ~43% and ~17% of both, EELGs primary (ID: 2532, 6465 and 7373) and extended (ID: 1699) samples, respectively, are included in this class.

Note that we applied a similar approach as Guérou et al. (2017) considering a galaxy spatially resolved if the galaxy has at least an area of 16 MUSE spaxels (i.e. about 1.5 times the PSF FWHM size of the data cube). We are aware that mergers may mimic the appearance of rotation patterns in observations of finite spatial resolution. Therefore, observations with better spatial resolution (e.g. JWST or MUSE-NFM observations) are necessary to reliably determine the internal structure of these systems.

4.3. Global properties and evolution

Figure 4 displays the relations among the derived [OIII] luminosity and velocity dispersion, stellar mass and SFR (both parameters taken from the AMUSED database, as derived using the Prospector code⁹), for both the primary and extended samples. Inspection of this figure first reveals that, when comparing the behaviour of both samples, no clear differences can be found between them, i.e. the EWo limits assumed to select our EELGs do not seem to introduce a bias in their observed properties. Overall, all four parameters show good correlations, with the SFR vs. stellar mass plot delineating a very clear main sequence for our sample of EELGs. From the ionized gas, the derived [OIII] line luminosity and σ correlate, showing both parameters some degree of correlation versus stellar mass and SFR -most notably between stellar mass and [OIII] luminosity-. This is relevant since we are comparing properties, e.g. [OIII] luminosity and stellar mass, which have been independently derived, corresponding to gaseous and stellar components of the EELG galaxies, respectively.

In Figure 6 we present the mass-metallicity relation showing average loci corresponding to nearby (SDSS) and high redshift galaxies. Our EELG galaxies¹⁰, sampling the low stellar mass ($\text{Mass}_{\text{pro}} \leq 9.0$) and low metallicity ($12+\log(\text{O}/\text{H}) \leq 8.0$) region of the plot, are consistent with the mass-metallicity relation derived for $z \sim 2.2$ (Sanders et al. 2016) galaxies. They are also close to the locus defined by very high-redshift objects ($z = 7.7\text{-}8.5$ and $z = 6.1\text{-}6.3$), as recently studied by Schaerer et al. (2022) and Sun et al. (2023) using JWST data. This result illustrates how the EELGs in our sample can be considered true local analogs of these high-redshift systems. The next generation of ground-based 30-meter telescopes, together with additional observations

⁹ All the details of the derivation of stellar mass and SFR can be found in Bacon et al. (2023)

¹⁰ Only eight of the galaxies in Table 3 have stellar mass values in the AMUSED database

from space, will allow us to fill this figure with low metallicity and low massive EELG galaxies at high-redshift and their local analogs.

5. Summary

During decades, the EELGs searches have been performed on broad-band photometry data. Recently, thanks to the development of new instruments and recent surveys such as SDSS or J-PAS, direct spectroscopy or narrow-band searches have been carried out (e.g. Indahl et al. 2021; Iglesias-Páramo et al. 2022). However, the number of EELG searches and analyses performed to date based on IFU data is (to our knowledge) very scarce. In fact, this work could be considered among the first EELG searches performed based on deep IFU data surveys, since previous works have studied mostly specific objects (e.g. Lofthouse et al. 2017; Bosch et al. 2019; Arroyo-Polonio et al. 2023).

Taking advantage of the deepest IFU survey to date, we present spatially resolved kinematic maps for a sample of intermediate redshift EELGs observed from ground. Furthermore, we confirm that these systems are true local analogs of high-redshift systems ($z=6-8$) studied by the JWST. While these cases already reveal the fantastic potential of the MUSE Ultra Deep Field data set, our small sample prevents a more detailed study on the basic properties of EELGs. However, this work can be regarded as a successful pilot study, demonstrating the power of the presented methodology to analyse strong emission-line galaxies using IFU data. Future deep observations with MUSE or on-going instrument such as HARMONI will result in a larger sample in which to apply the methodology presented here.

Acknowledgements. We thank the referee for carefully reading our manuscript and providing constructive comments improving the paper. This study uses data provided by the MUSE Hubble Ultra Deep survey, publicly available at the AMUSED database¹¹. IMC acknowledges funding from U. La Laguna through the Margarita Salas Fellowship from the Spanish Ministry of Universities ref. UNI/551/2021-May 26 and under the EU Next Generation funds, and from ANID programme FONDECYT Postdoctorado 3230653. JMV, JIP, AAP acknowledge financial support from grants CEX2021-001131-S and PID2019-107408GB-C44 funded by MCIN/AEI/ 10.13039/501100011033. This paper makes use of python¹²; Matplotlib (Hunter 2007): a suite of open-source python modules that provide a framework for creating scientific plots; Astropy¹³: a community-developed core Python package and an ecosystem of tools and resources for astronomy (Astropy Collaboration et al. 2013, 2018, 2022); MPDAP¹⁴: an open-source Python package that provides tools to work with MUSE-specific data; and pyplatefit¹⁵ (Bacon et al. 2023): a python routine for emission and absorption lines fit of MUSE spectra. and AMUSED¹⁶: a public web interface for inspection and retrieval of extragalactic MUSE data products. IMC thank Alejandro S. Borlaff for helpful discussions on the HST broad-band images.

References

Amorín, R., Pérez-Montero, E., Contini, T., et al. 2015, A&A, 578, A105
 Amorín, R., Vílchez, J. M., Hägele, G. F., et al. 2012, ApJ, 754, L22
 Amorín, R. O., Pérez-Montero, E., & Vílchez, J. M. 2010, ApJ, 715, L128
 Andrews, B. H. & Martini, P. 2013, ApJ, 765, 140
 Arroyo-Polonio, A., Iglesias-Páramo, J., Kehrig, C., et al. 2023, A&A, 677, A114
 Astropy Collaboration, Price-Whelan, A. M., Lim, P. L., et al. 2022, apj, 935, 167

Astropy Collaboration, Price-Whelan, A. M., Sipőcz, B. M., et al. 2018, AJ, 156, 123
 Astropy Collaboration, Robitaille, T. P., Tollerud, E. J., et al. 2013, A&A, 558, A33
 Bacon, R., Brinchmann, J., Conseil, S., et al. 2023, A&A, 670, A4
 Bacon, R., Conseil, S., Mary, D., et al. 2017, A&A, 608, A1
 Barrera-Ballesteros, J. K., Falcón-Barroso, J., García-Lorenzo, B., et al. 2014, A&A, 568, A70
 Beckwith, S. V. W., Stiavelli, M., Koekemoer, A. M., et al. 2006, AJ, 132, 1729
 Bekki, K. 2015, MNRAS, 454, L41
 Bergvall, N., Zackrisson, E., Andersson, B. G., et al. 2006, A&A, 448, 513
 Bittner, A., Falcón-Barroso, J., Nedelchev, B., et al. 2019, A&A, 628, A117
 Bosch, G., Hägele, G. F., Amorín, R., et al. 2019, MNRAS, 489, 1787
 Brinchmann, J., Charlot, S., White, S. D. M., et al. 2004, MNRAS, 351, 1151
 Bruzual, G. & Charlot, S. 2003, MNRAS, 344, 1000
 Cardamone, C., Schawinski, K., Sarzi, M., et al. 2009, MNRAS, 399, 1191
 Cardelli, J. A., Clayton, G. C., & Mathis, J. S. 1989, ApJ, 345, 245
 Dayal, P. & Ferrara, A. 2018, Phys. Rep., 780, 1
 del Moral-Castro, I., García-Lorenzo, B., Ramos Almeida, C., et al. 2019, MNRAS, 485, 3794
 del Moral-Castro, I., García-Lorenzo, B., Ramos Almeida, C., et al. 2020, A&A, 639, L9
 Domínguez-Gómez, J., Pérez, I., Ruiz-Lara, T., et al. 2023, Nature, 619, 269
 Duarte Puertas, S., Vilchez, J. M., Iglesias-Páramo, J., et al. 2022, A&A, 666, A186
 Erb, D. K., Pettini, M., Steidel, C. C., et al. 2016, ApJ, 830, 52
 Fletcher, T. J., Tang, M., Robertson, B. E., et al. 2019, ApJ, 878, 87
 Guérou, A., Krajnović, D., Epinat, B., et al. 2017, A&A, 608, A5
 Haro, G. 1956, Boletín de los Observatorios Tonantzintla y Tacubaya, 2, 8
 Harshan, A., Gupta, A., Tran, K.-V., et al. 2020, ApJ, 892, 77
 Hunter, J. D. 2007, Computing in Science & Engineering, 9, 90
 Iglesias-Páramo, J., Arroyo, A., Kehrig, C., et al. 2022, A&A, 665, A95
 Inami, H., Bacon, R., Brinchmann, J., et al. 2017, A&A, 608, A2
 Indahl, B., Zeimann, G., Hill, G. J., et al. 2021, ApJ, 916, 11
 Izotov, Y. I., Guseva, N. G., Fricke, K. J., & Henkel, C. 2019, A&A, 623, A40
 Izotov, Y. I., Schaerer, D., Thuan, T. X., et al. 2016, MNRAS, 461, 3683
 Izotov, Y. I., Wörseck, G., Schaerer, D., et al. 2018, MNRAS, 478, 4851
 Jaskot, A. E. & Oey, M. S. 2013, ApJ, 766, 91
 Kehrig, C., Vilchez, J. M., Pérez-Montero, E., et al. 2016, MNRAS, 459, 2992
 Lagos, P., Demarco, R., Papaderos, P., et al. 2016, MNRAS, 456, 1549
 Lofthouse, E. K., Houghton, R. C. W., & Kaviraj, S. 2017, MNRAS, 471, 2311
 Lumbreras-Calle, A., López-Sanjuan, C., Sobral, D., et al. 2022, A&A, 668, A60
 Markarian, B. E. 1967, Astrofizika, 3, 24
 Matthee, J., Naidu, R. P., Pezzulli, G., et al. 2022, MNRAS, 512, 5960
 Naidu, R. P., Matthee, J., Oesch, P. A., et al. 2022, MNRAS, 510, 4582
 Paalvast, M., Verhamme, A., Straka, L. A., et al. 2018, A&A, 618, A40
 Pagel, B. E. J., Edmunds, M. G., Blackwell, D. E., Chun, M. S., & Smith, G. 1979, MNRAS, 189, 95
 Pérez-Montero, E. 2017, PASP, 129, 043001
 Pérez-Montero, E., Amorín, R., Sánchez Almeida, J., et al. 2021, MNRAS, 504, 1237
 Pérez-Montero, E., Kehrig, C., Vilchez, J. M., et al. 2020, A&A, 643, A80
 Ravindranath, S., Monroe, T., Jaskot, A., Ferguson, H. C., & Tumlinson, J. 2020, ApJ, 896, 170
 Relaño, M., Monreal-Ibero, A., Vilchez, J. M., & Kennicutt, R. C. 2010, MNRAS, 402, 1635
 Roche, N., Vilchez, J. M., Iglesias-Páramo, J., et al. 2023, MNRAS, 523, 270
 Salzer, J. J., Feddersen, J. R., Derloshon, K., et al. 2020, AJ, 160, 242
 Sanders, R. L., Shapley, A. E., Kriek, M., et al. 2016, ApJ, 816, 23
 Schaerer, D., Marques-Chaves, R., Barrufet, L., et al. 2022, A&A, 665, L4
 Schlafly, E. F. & Finkbeiner, D. P. 2011, ApJ, 737, 103
 Stark, D. P. 2016, ARA&A, 54, 761
 Storey, P. J. & Hummer, D. G. 1995, MNRAS, 272, 41
 Sun, F., Egami, E., Pirzkal, N., et al. 2023, ApJ, 953, 53
 Tang, M., Stark, D. P., Chevallard, J., et al. 2021, MNRAS, 503, 4105
 Terlevich, R., Melnick, J., Masegosa, J., Moles, M., & Copetti, M. V. F. 1991, A&AS, 91, 285
 Williams, H., Kelly, P. L., Chen, W., et al. 2023, Science, 380, 416
 Yang, H., Malhotra, S., Gronke, M., et al. 2017a, ApJ, 844, 171
 Yang, H., Malhotra, S., Rhoads, J. E., & Wang, J. 2017b, ApJ, 847, 38
 Zwicky, F. 1966, ApJ, 143, 192

¹¹ <https://amused.univ-lyon1.fr/>

¹² <http://www.python.org>

¹³ <http://www.astropy.org>

¹⁴ <https://mpdaf.readthedocs.io>

¹⁵ <https://github.com/musevlt/pyplatefit>

¹⁶ <https://amused.univ-lyon1.fr/>

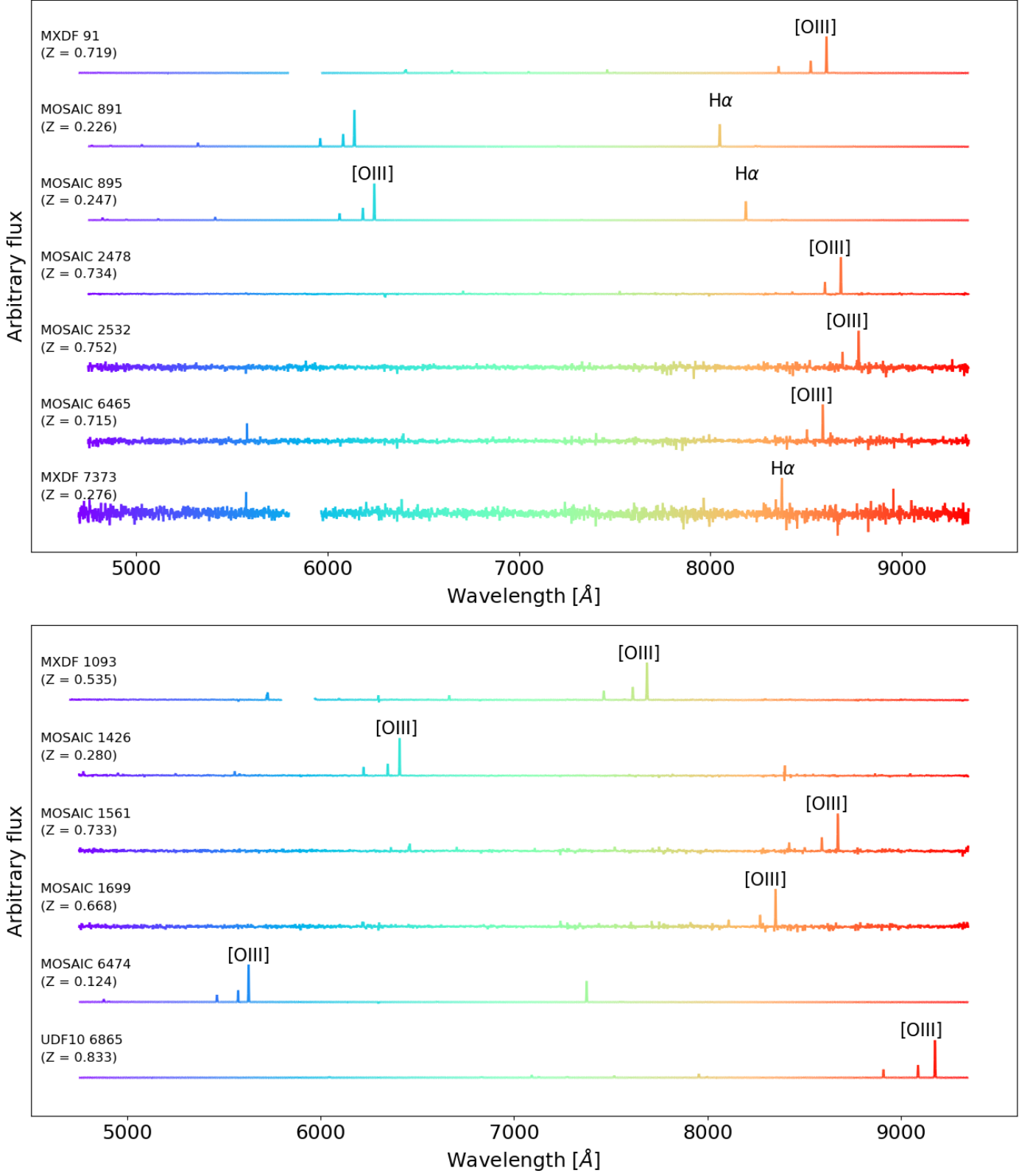


Fig. 2. Spectra for both our primary (*top panel*) and extended (*bottom panel*) EELG samples. MUSE ID, data set, redshift and emission line used for the classification are indicated for each spectra.

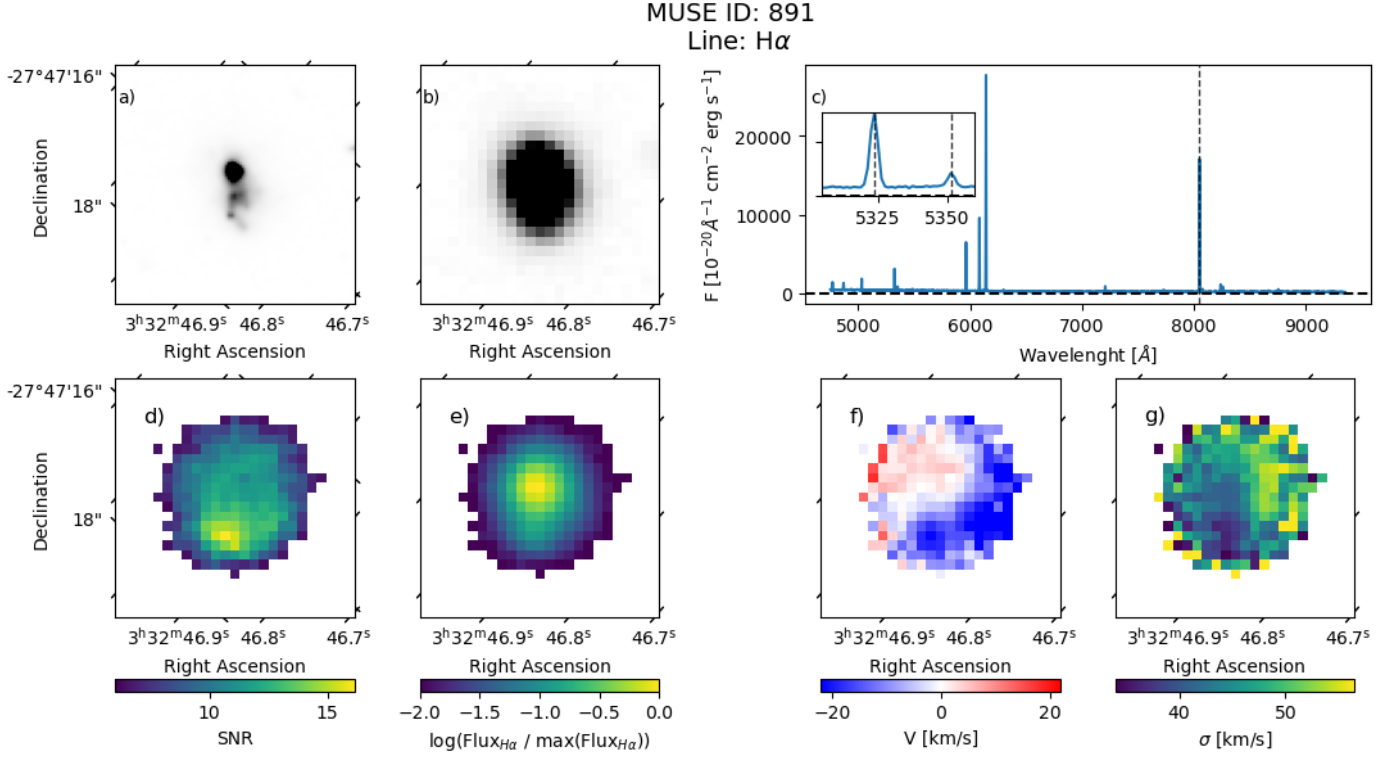


Fig. 3. MUSE ID 891: a) HST F775W image with the spatial coverage of the MUSE data cube; b) MUSE *white light* image of the galaxy; c) spectrum of the object with an inset window showing a zoom around the H γ and [OIII] λ 4363 emission lines; maps of d) SNR, e) **normalised** flux, f) relative radial velocity, and g) velocity dispersion (σ), for the emission line indicated in the figure header.

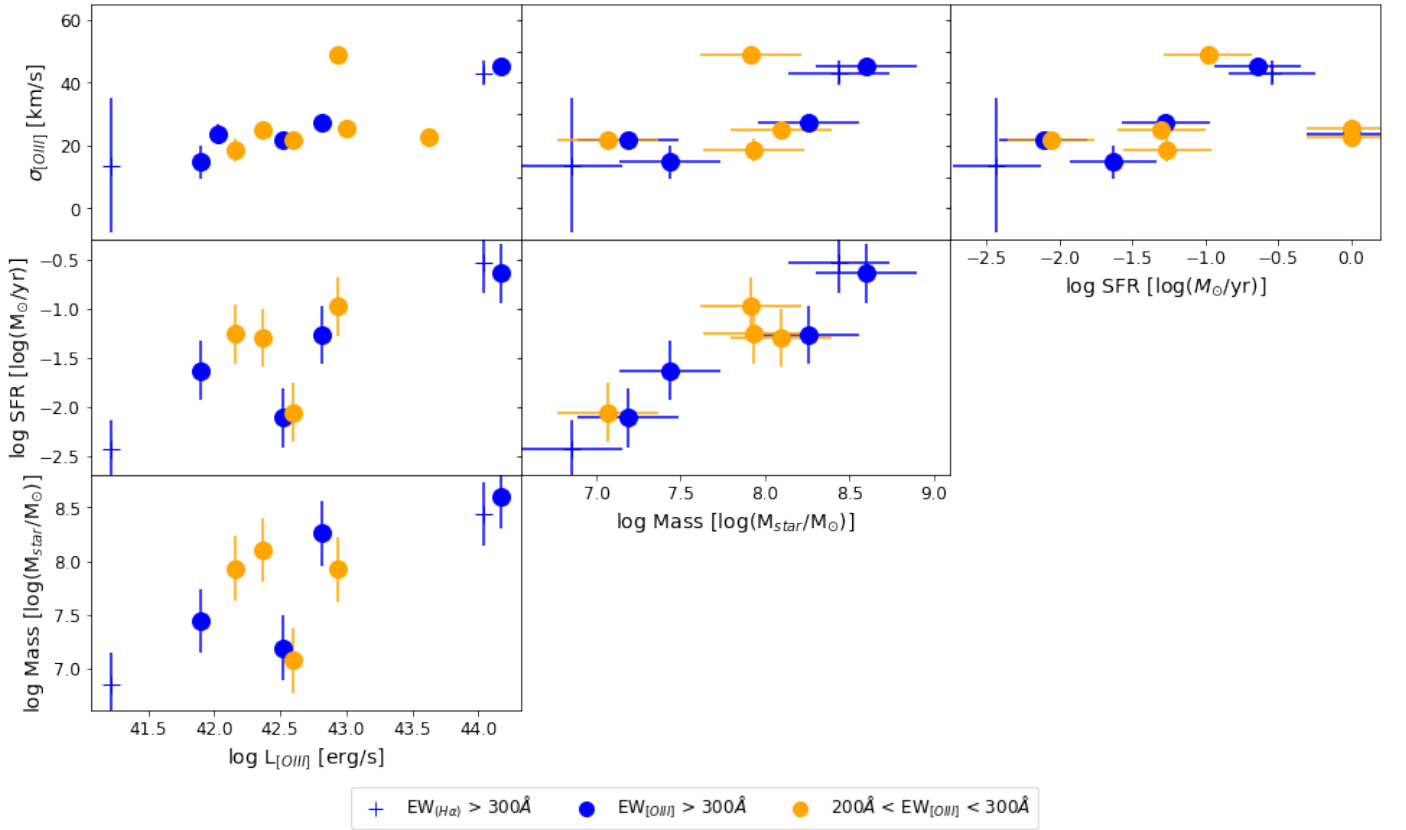


Fig. 4. Correlations between the luminosity, stellar mass, star formation rate and σ_{OIII} . We assume typical uncertainties of 0.3dex for mass and star formation rate (see Bacon et al. 2023).

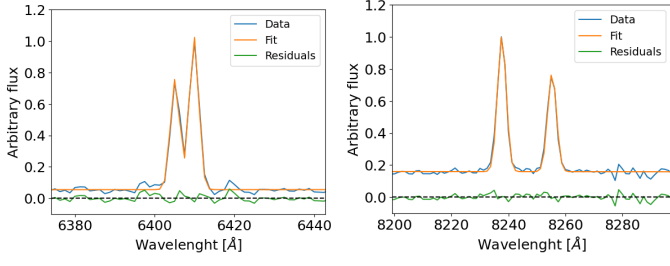


Fig. 5. Electron density sensitive lines. *Left panel:* fit to the [OII] $\lambda\lambda 3726, 3729$ doublet in the spectrum of galaxy ID 91. *Right panel:* fit to the [SII] $\lambda\lambda 6717, 6731$ doublet in the spectrum of galaxy ID 891. In each plot, the observed spectrum (blue) and its fit (orange), and the residuals (green), are shown.

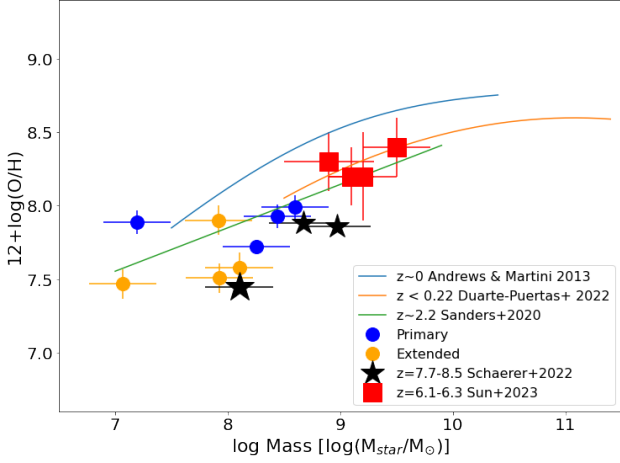


Fig. 6. Mass-metallicity relation. Oxygen chemical abundance and stellar mass for the galaxies in the primary (blue circles) and extended (orange circles) samples in this work, compared to mean relations observed at $z \sim 0$ (Andrews & Martini 2013), $z < 0.22$ (Duarte Puertas et al. 2022), and $z \sim 2.2$ (Sanders et al. 2016). Black stars and red squares show recent results for high-redshift galaxies from JWST data (Schaerer et al. 2022; Sun et al. 2023).

Appendix A: Spectra and images of the primary EELG sample candidates

In this appendix, we show both the spectra and the images of the selected EELG candidates.

Appendix B: Spectra and images of the EELG extended sample

Here, we present both the spectra and the images of the extended sample.

Appendix C: Line fluxes of the EELG primary sample candidates

In this appendix, we show the fluxes and equivalent width measured with pyPlatefit for our EELG sample. Only lines with SNR higher than 3 are included in the tables.

Appendix D: Line fluxes of the EELG extended sample candidates

Here, we present the fluxes and equivalent width measured with pyPlatefit for our extended sample. Only lines with SNR higher than 3 are included in the tables.

MUSE ID: 895
Line: [OIII]5007 and H α

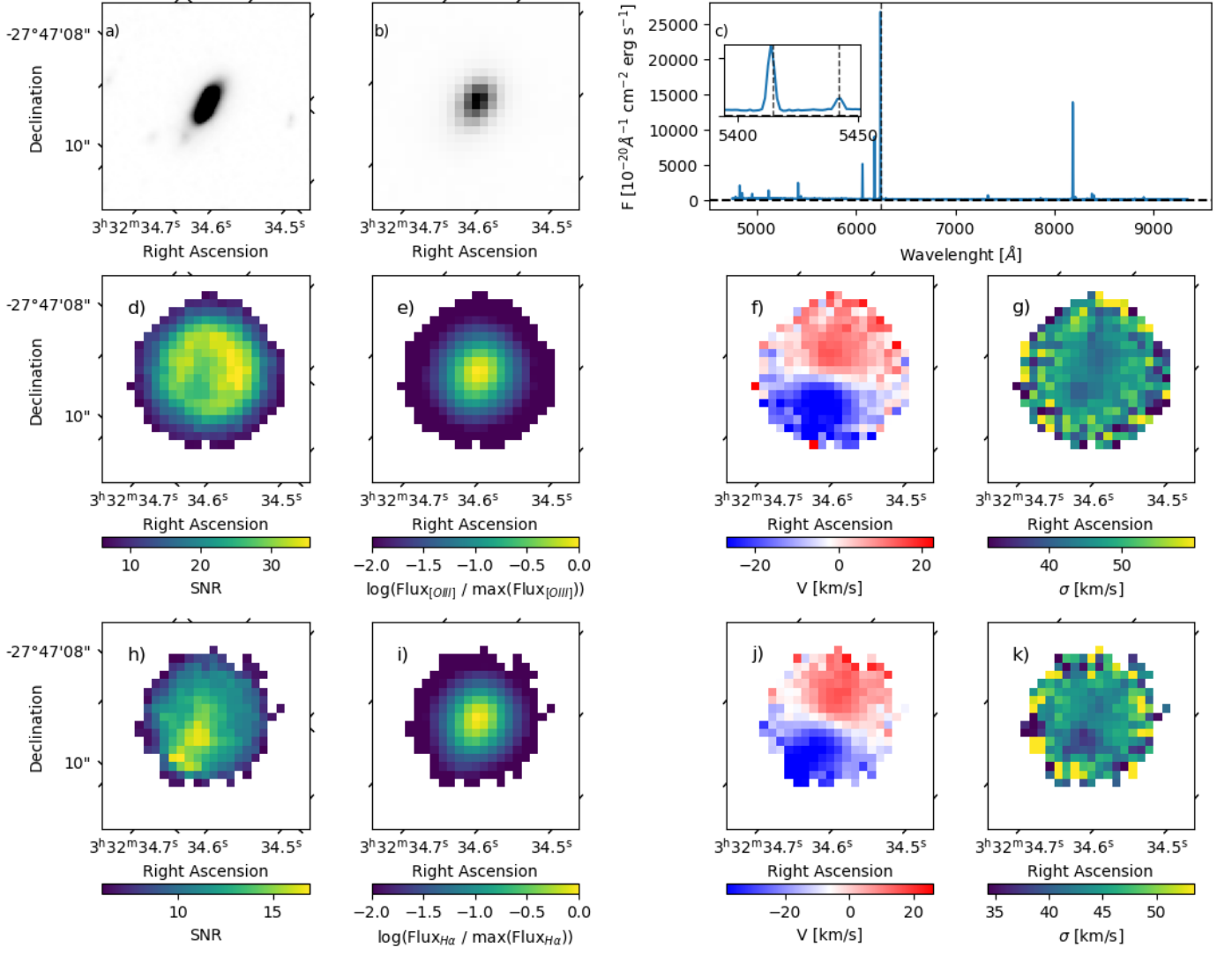


Fig. A.1. Same as Fig. 3 for the MUSE ID galaxy 895.

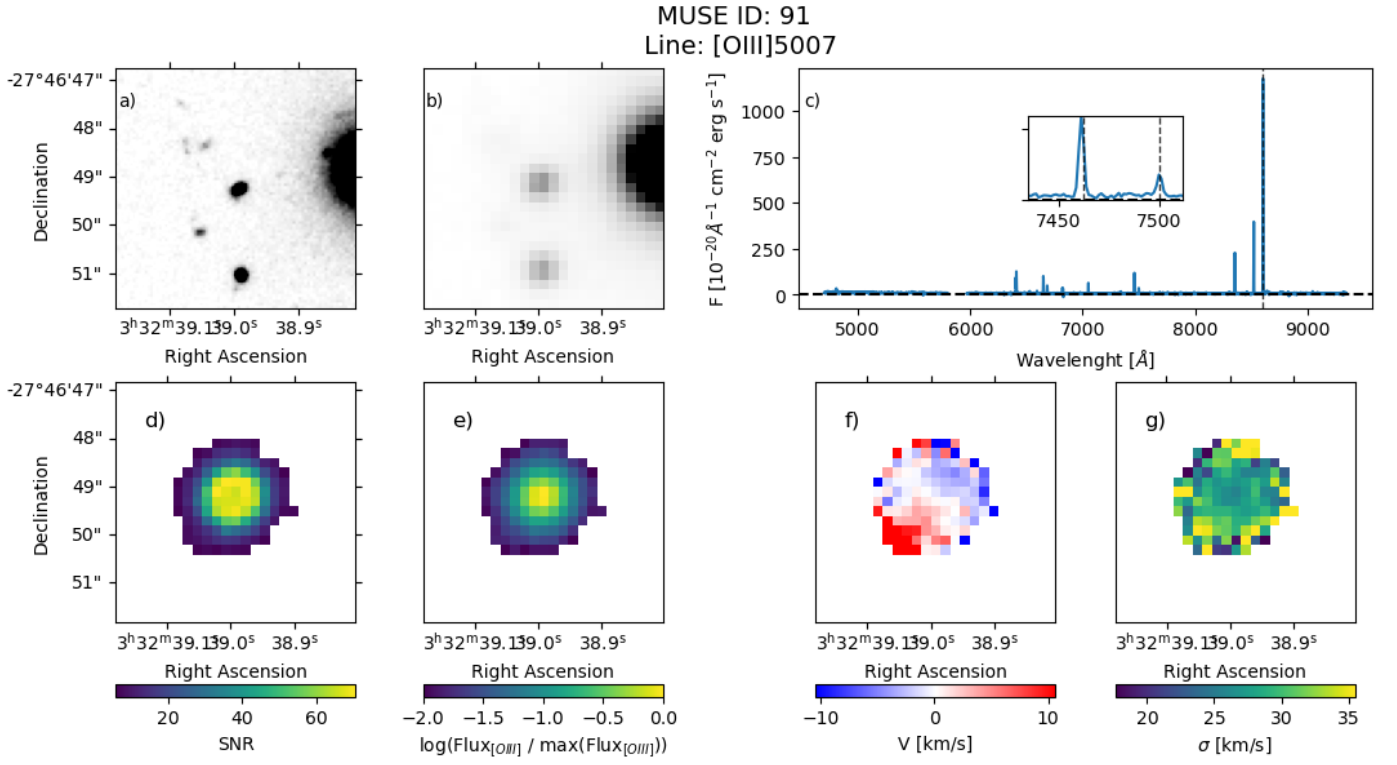


Fig. A.2. Same as Fig. 3 for the MUSE ID galaxy 91.

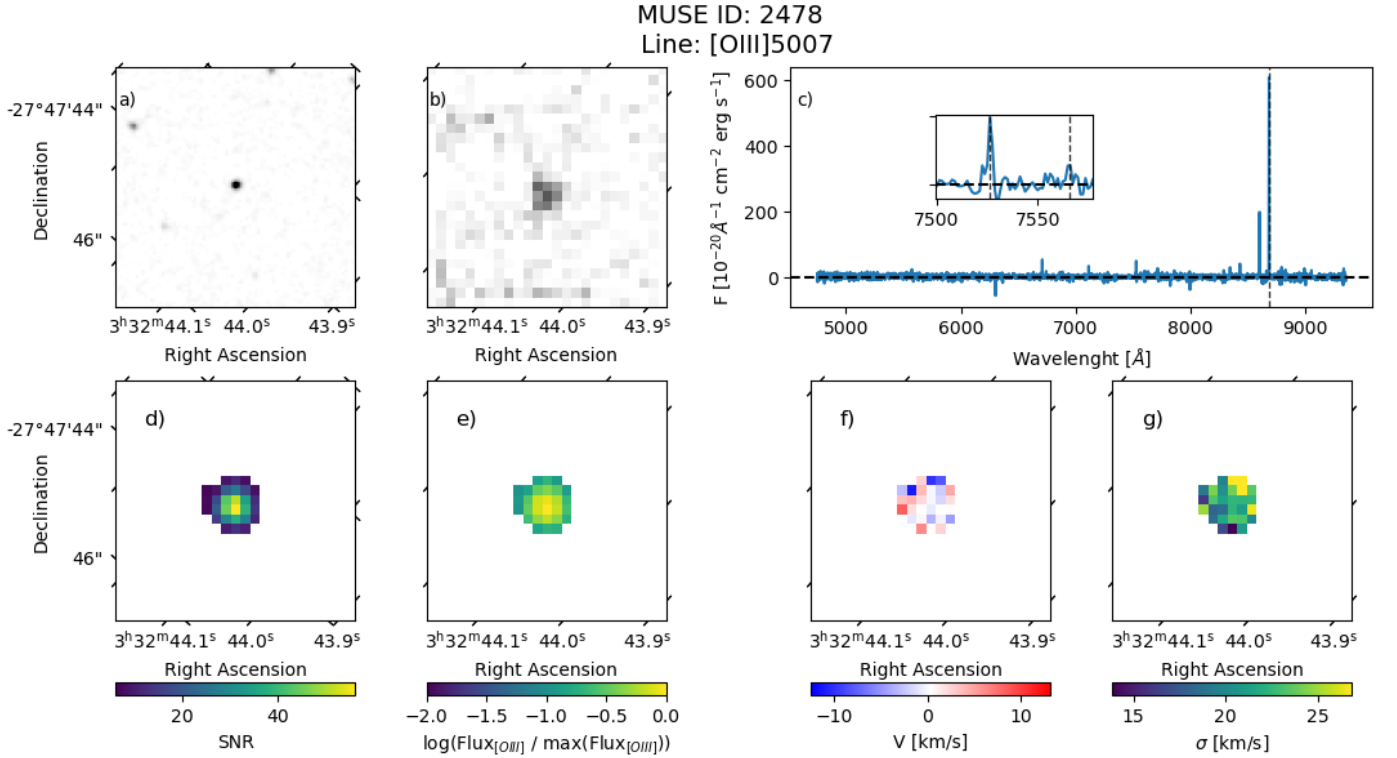


Fig. A.3. Same as Fig. 3 for the MUSE ID galaxy 2478.

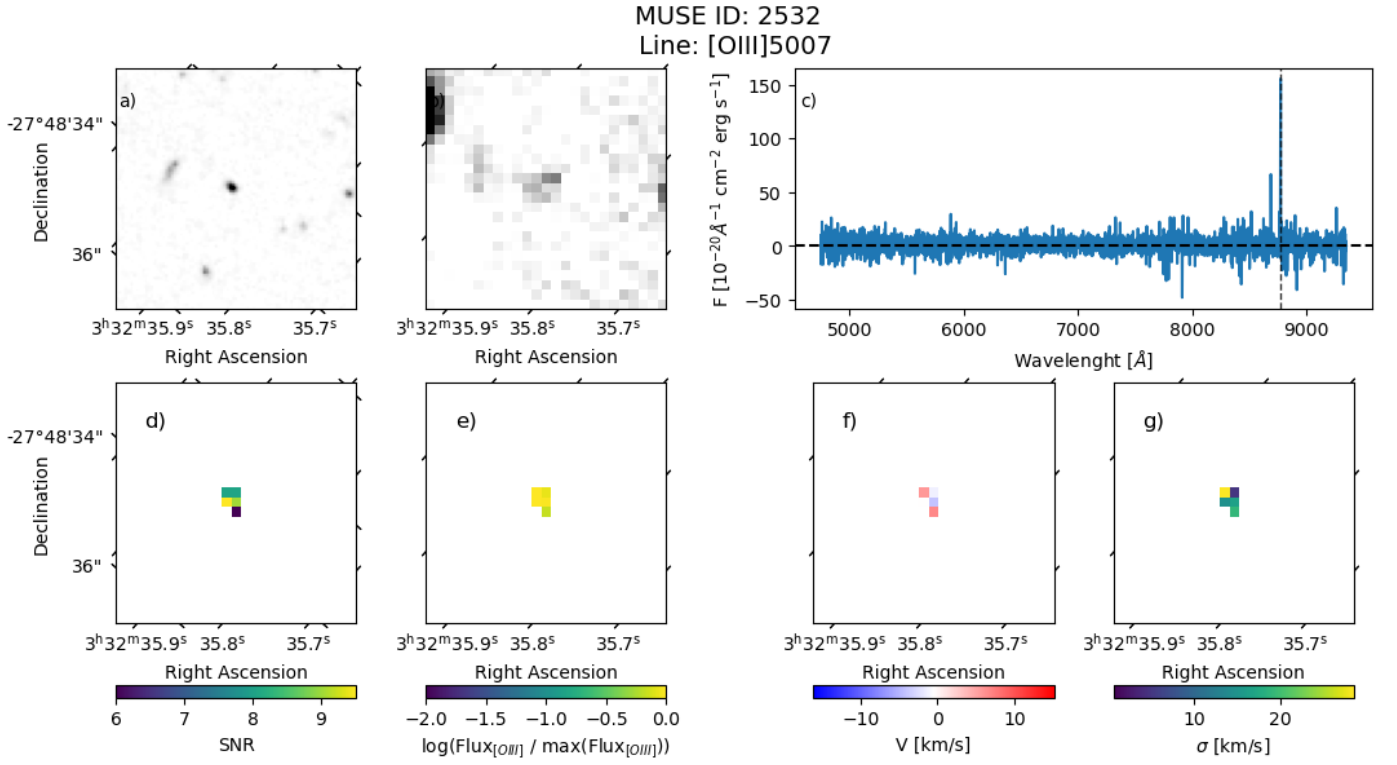


Fig. A.4. Same as Fig. 3 for the MUSE ID galaxy 2532.

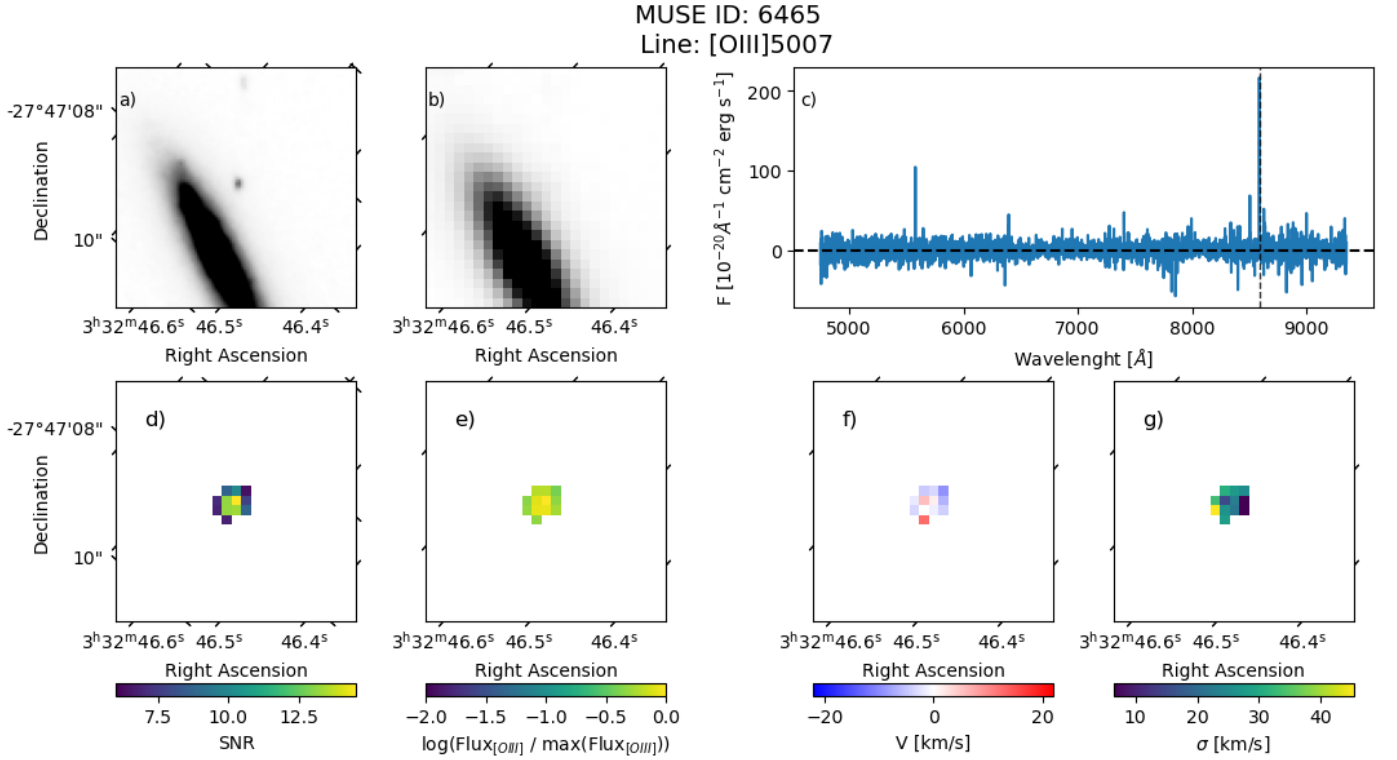


Fig. A.5. Same as Fig. 3 for the MUSE ID galaxy 6465.

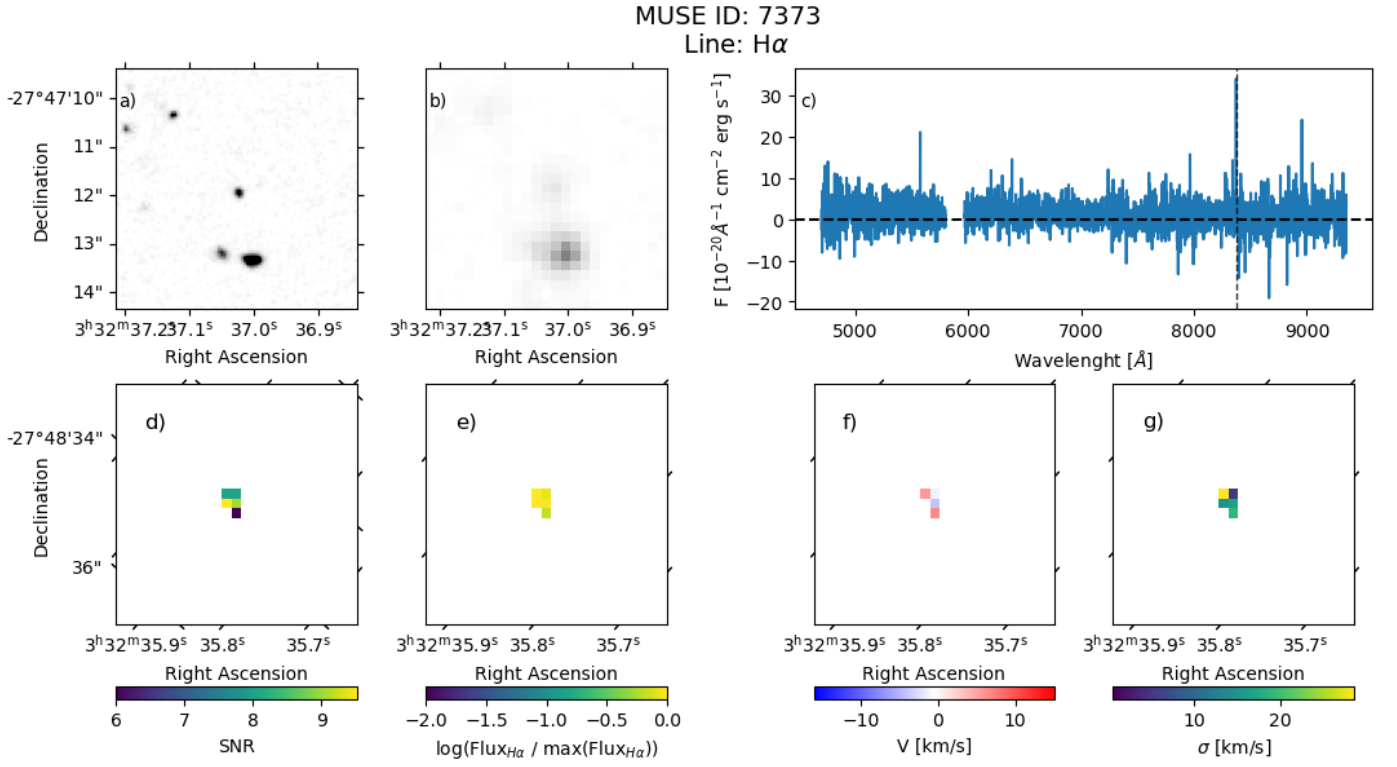


Fig. A.6. Same as Fig. 3 for the MUSE ID galaxy 7373.

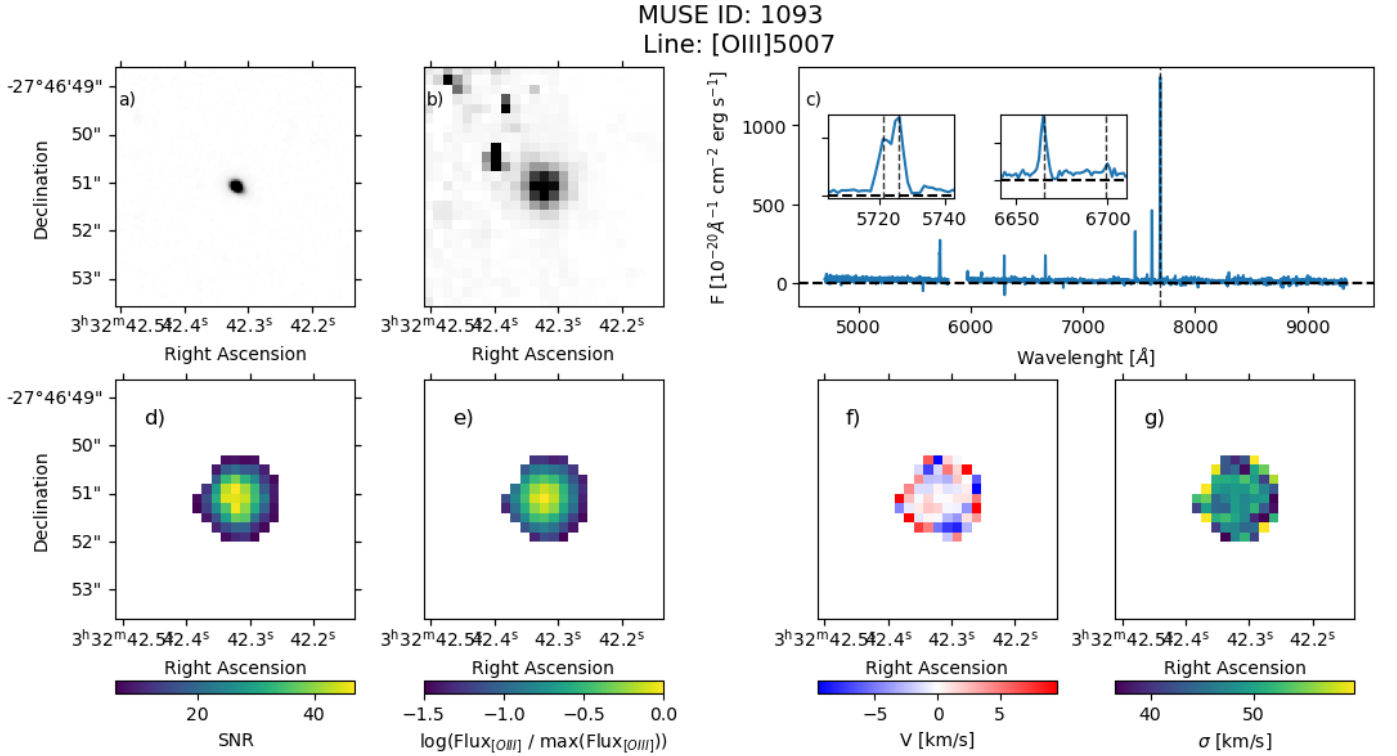


Fig. B.1. Same as Fig. 3 for the MUSE ID galaxy 1093.

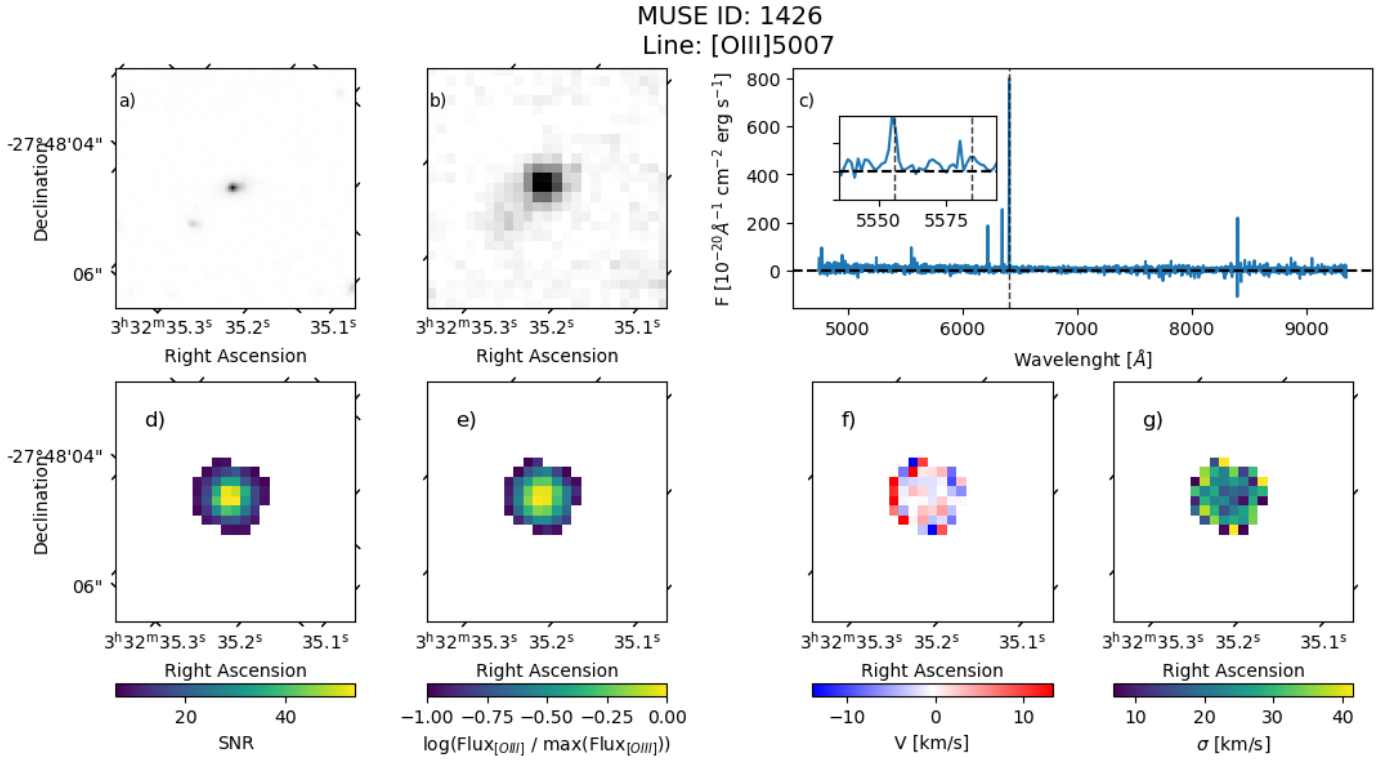


Fig. B.2. Same as Fig. 3 for the MUSE ID galaxy 1426.

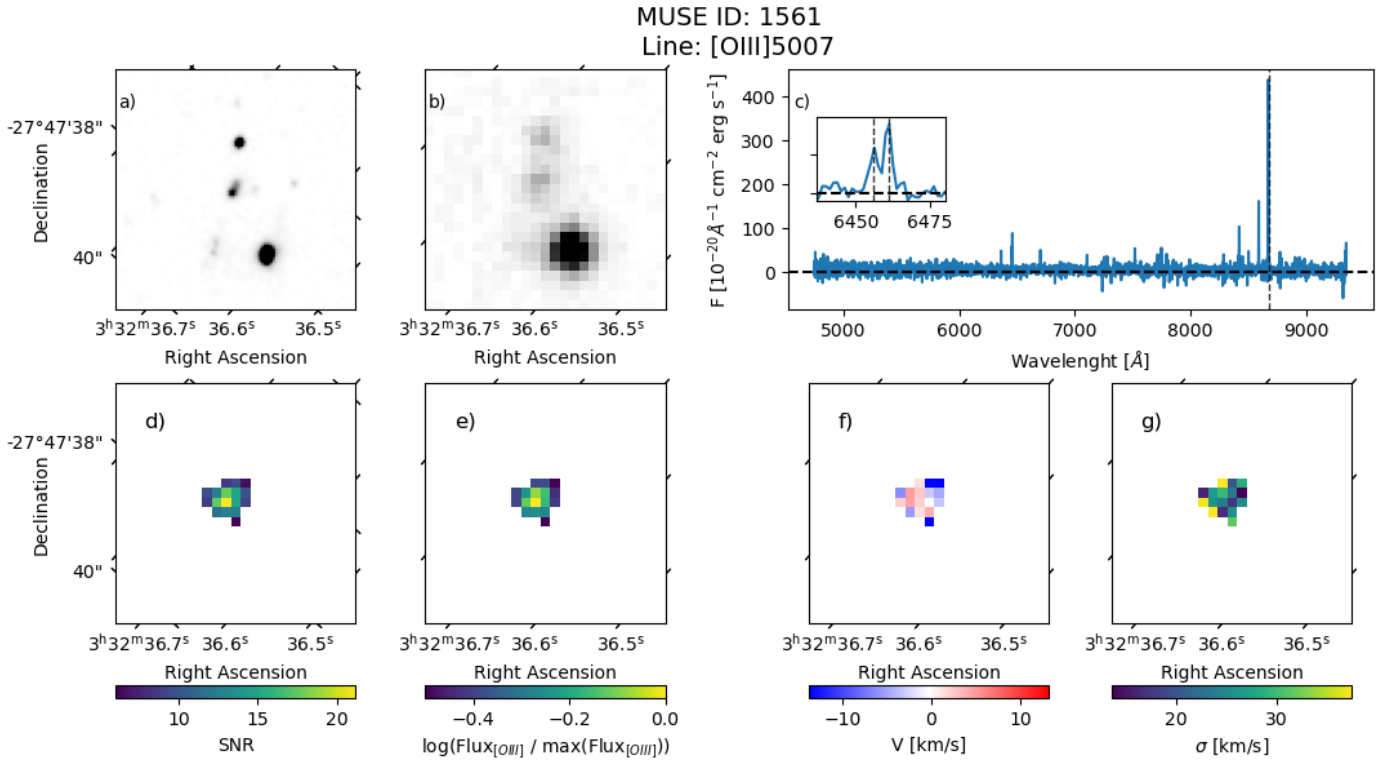


Fig. B.3. Same as Fig. 3 for the MUSE ID galaxy 1561.

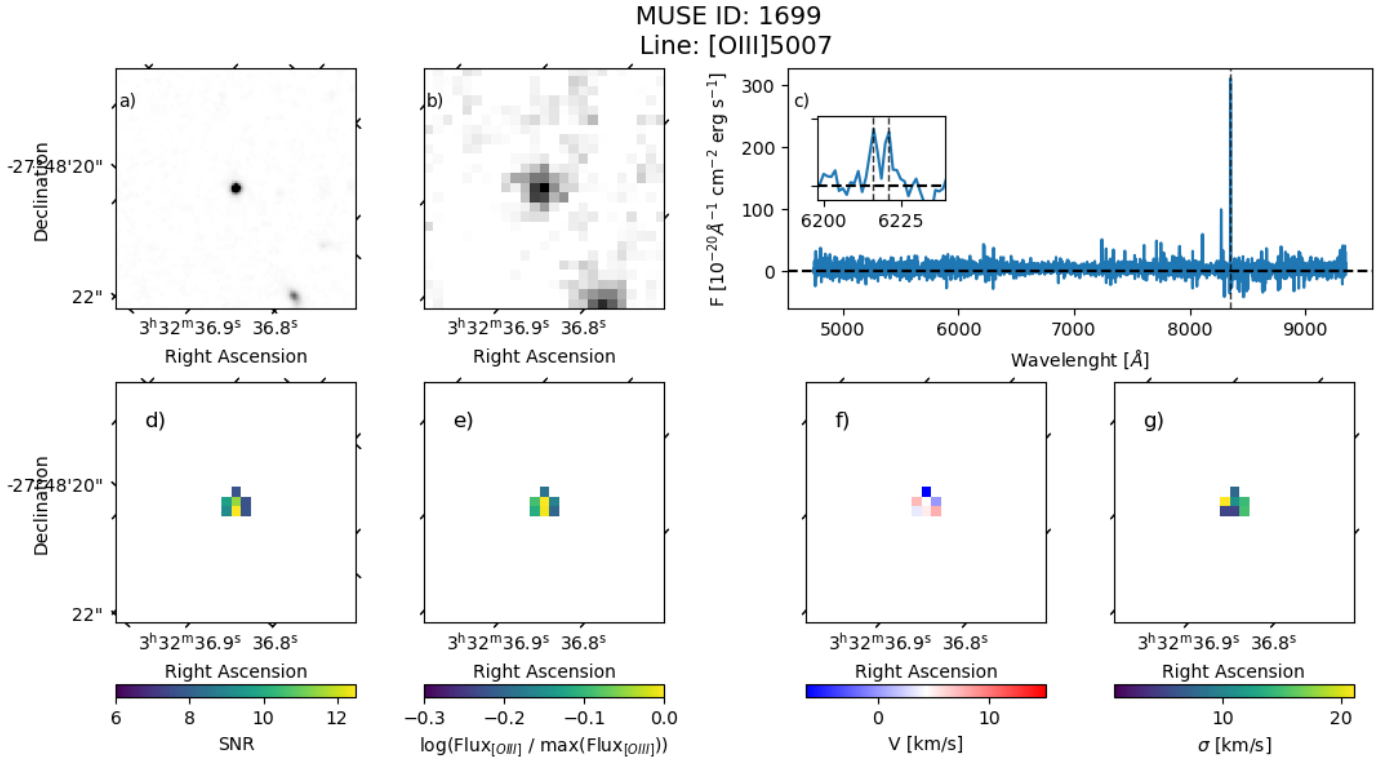


Fig. B.4. Same as Fig. 3 for the MUSE ID galaxy 1699.

Galaxy ID	91	891	895	2478	2532	6465	7373
Line	λ (Å)	F ($10^{-20} \frac{\text{erg}}{\text{scm}^2}$)	F ($10^{-20} \frac{\text{erg}}{\text{scm}^2}$)	F ($10^{-20} \frac{\text{erg}}{\text{scm}^2}$)	F ($10^{-20} \frac{\text{erg}}{\text{scm}^2}$)	F ($10^{-20} \frac{\text{erg}}{\text{scm}^2}$)	F ($10^{-20} \frac{\text{erg}}{\text{scm}^2}$)
(1)	(2)	(3)	(4)	(5)	(6)	(7)	(8)
[OII]	3726.03	257 ± 7	94 ± 2
[OII]	3728.82	356 ± 5	125 ± 3
H11	3770.63	21 ± 5
H10	3797.90	41 ± 4
H9	3835.39	52 ± 3	...	1347 ± 34
[NeIII]	3868.75	277 ± 8	...	6342 ± 8	135 ± 4	38 ± 4	54 ± 2
[HeI]	3888.65	132 ± 3	4266 ± 8	3298 ± 28	48 ± 2
H8	3889.05	134 ± 5	4213 ± 8	3264 ± 28	47 ± 2
[NeIII]	3967.46	95 ± 3	3588 ± 11	2940 ± 9
Hε	3970.07	98 ± 6	4016 ± 9	3209 ± 11	49 ± 4
Hδ	4101.74	196 ± 4	5757 ± 6	4515 ± 27	92 ± 4
Hγ	4340.47	354 ± 5	9956 ± 7	8167 ± 18	142 ± 2	...	62 ± 5
[OIII]	4363.21	91 ± 5	1609 ± 8	1399 ± 12	39 ± 4
Hβ	4861.33	779 ± 8	21673 ± 10	18180 ± 16	162 ^a	109 ± 3	102 ± 9
[OIII]	4958.91	1364 ± 3	32476 ± 16	30788 ± 5	583 ± 3	198 ± 2	158 ± 7
[OIII]	5006.84	4099 ± 6	95521 ± 16	92673 ± 17	2065 ± 3	492 ± 3	668 ± 6
[HeI]	5875.67	...	2387 ± 13	2119 ± 6
[OI]	6300.30	...	851 ± 7	851 ± 8
Hα	6562.82	...	67942 ± 15	57500 ± 9	102 ± 2
[NII]	6583.41	...	1356 ± 8	1404 ± 11
[SII]	6716.47	...	3614 ± 8	3302 ± 10
[SII]	6730.85	...	2638 ± 9	2463 ± 5
[ArIII]	7135.78	...	1302 ± 6	1464 ± 10

Table C.1. Observed line fluxes for the primary sample. (1) Emission line; (2) Rest-frame wavelength; (3) Observed line fluxes for ID 91; (4) Observed line fluxes for ID 891; (5) Observed line fluxes for ID 895; (6) Observed line fluxes for ID 2478; (7) Observed line fluxes for ID 2532; (8) Observed line fluxes for ID 6465; (9) Observed line fluxes for ID 7373.

^a Uncertain value.

MUSE ID: 6474
Line: [OIII]5007 and H α

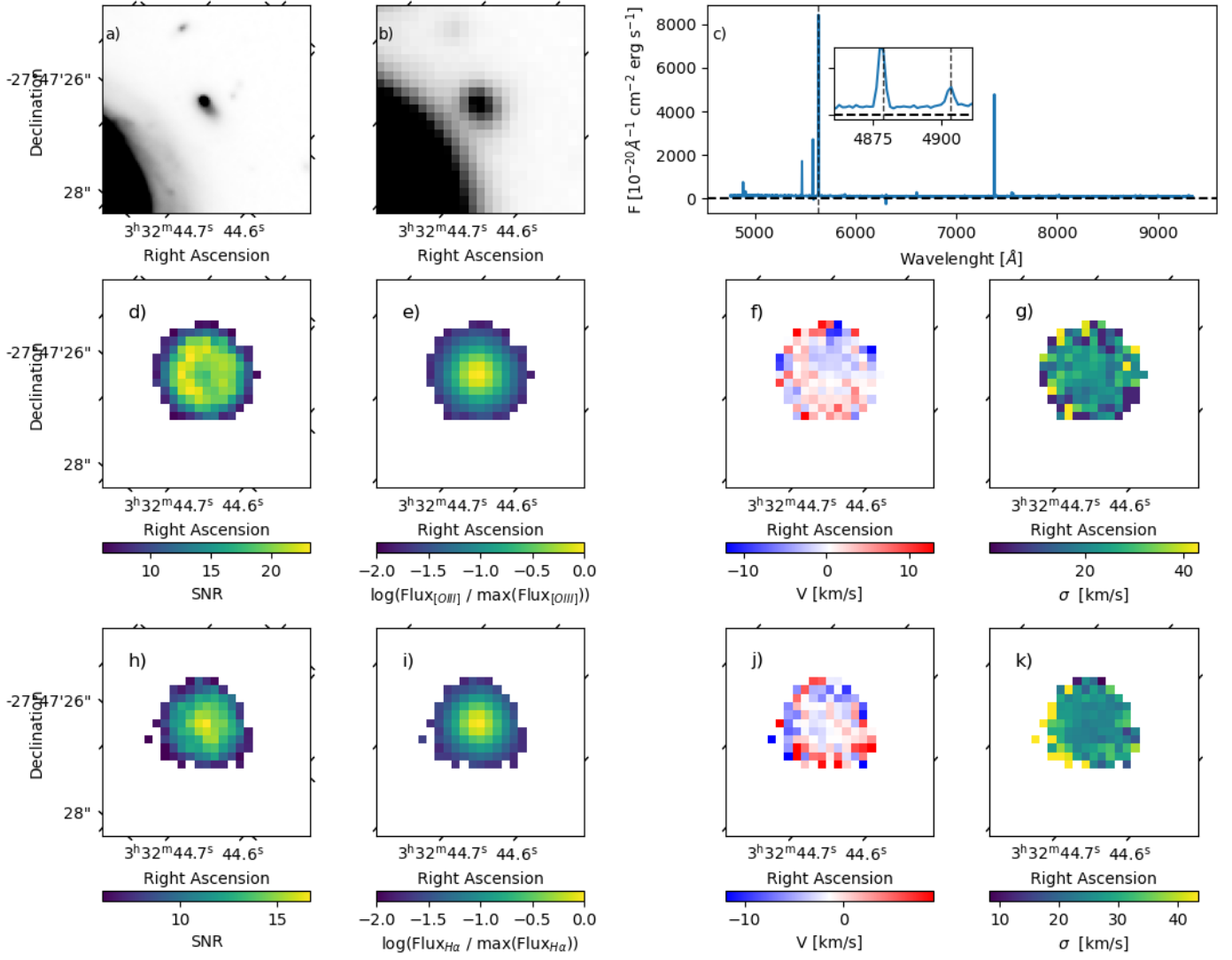


Fig. B.5. Same as Fig. 3 for the MUSE ID galaxy 6474.

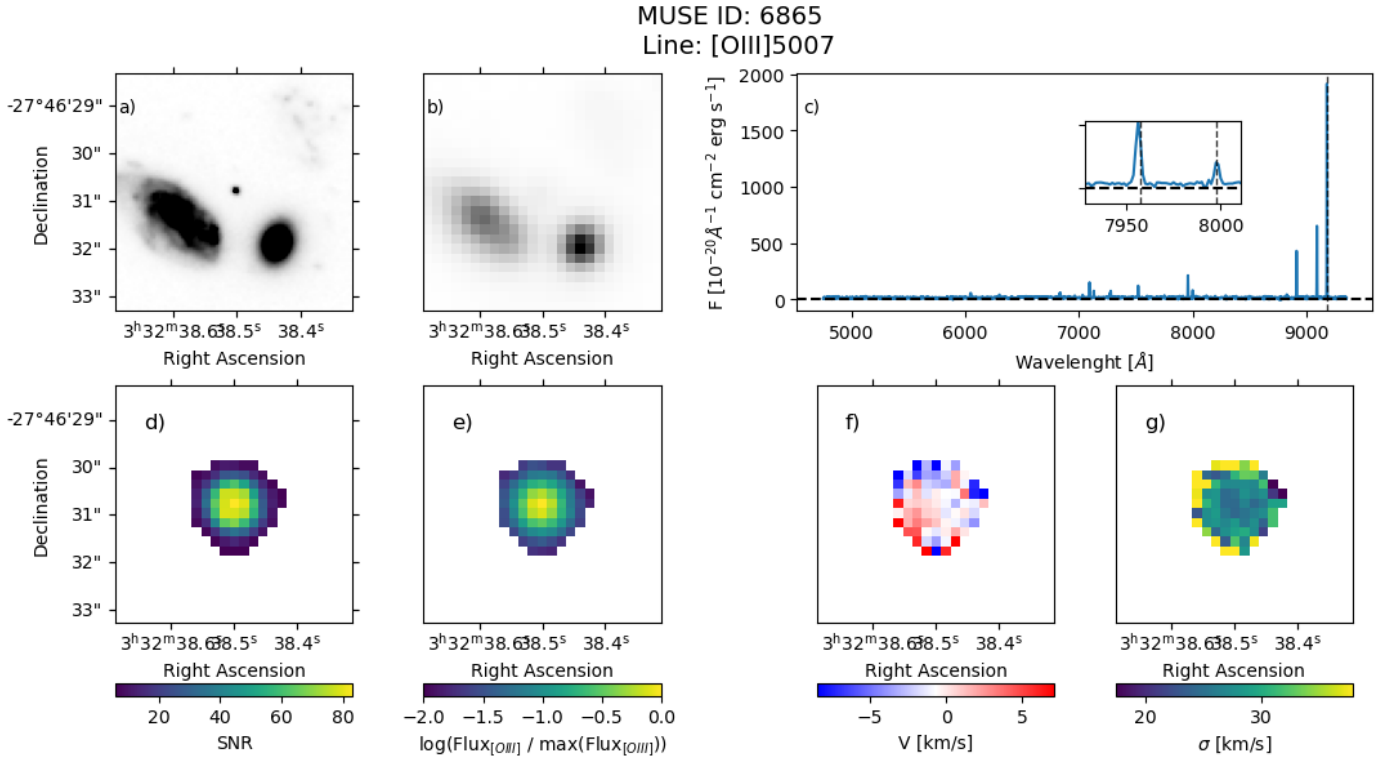


Fig. B.6. Same as Fig. 3 for the MUSE ID galaxy 6865.

Galaxy ID	1093	1426	1561	1699	6474	6865
Line	λ	F	F	F	F	F
	(Å)	$(10^{-20} \frac{\text{erg}}{\text{scm}^2})$	$(10^{-20} \frac{\text{erg}}{\text{scm}^2})$	$(10^{-20} \frac{\text{erg}}{\text{scm}^2})$	$(10^{-20} \frac{\text{erg}}{\text{scm}^2})$	$(10^{-20} \frac{\text{erg}}{\text{scm}^2})$
(1)	(2)	(3)	(4)	(5)	(6)	(7)
[MgII]	2795.53	57 ± 3
[OII]	3726.03	673 ± 6	107 ± 4	164 ± 4	107 ± 3	132 ± 3
[OII]	3728.82	981 ± 6	274 ± 4	262 ± 4	102 ± 3	126 ± 3
H11	3770.63	61 ± 3
H10	3797.90	78 ± 3
H9	3835.39	102 ± 2
[NeII]	3868.75	...	175 ± 3	135 ± 4	52 ± 3	382 ± 2
[HeI]	3888.65	...	98 ± 3	214 ± 2
H8	3889.05	...	112 ± 4	63 ± 4	...	220 ± 2
[NeII]	3967.46	185 ± 6	166 ± 3
Hε	3970.07	243 ± 7	93 ± 4	222 ± 4
Hδ	4101.74	489 ± 8	154 ± 4	103 ± 5	55 ± 4	347 ± 3
Hγ	4340.47	620 ± 7	276 ± 4	175 ± 5	...	659 ± 3
[OIII]	4363.21	75 ± 6	208 ± 2
Hβ	4861.33	1347 ± 9	626 ± 4	352 ± 6	221 ± 5	1453 ± 3
[OIII]	4958.91	1807 ± 7	771 ± 3	484 ± 4	309 ± 4	2054 ± 2
[OIII]	5006.84	5364 ± 9	2485 ± 5	1450 ± 6	905 ± 5	6276 ± 3
[HeI]	5875.67	135 ± 7	53 ± 3
[OI]	6300.30
Hα	6562.82
[NII]	6583.41
[SII]	6716.47
[SII]	6730.85
[ArIII]	7135.78

Table D.1. Same as Table C.1 for the extended sample. ^a Uncertain value.